J. Fluid Mech. (2024), *vol*. 980, A44, doi:10.1017/jfm.2024.23

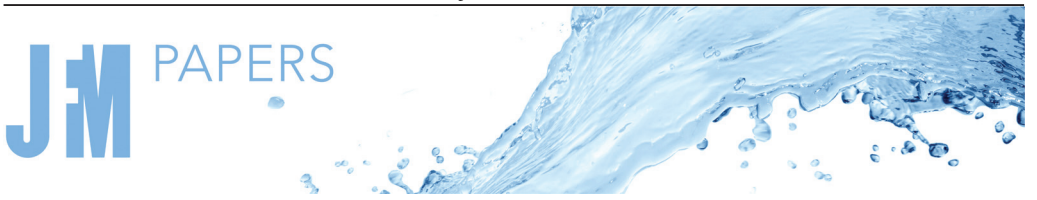

On the interfacial instabilities of a ventilation cavity induced by gaseous injection into liquid crossflow

Chengwang Xiong[1], Shengzhu Wang[1,2], Qianqian Dong[1,3], Shi-Ping Wang[1] and A-Man Zhang[1,†]

[1]College of Shipbuilding Engineering, Harbin Engineering University, Harbin 150001, PR China

[2]Marine Design and Research Institute of China, Shanghai 200011, PR China

[3]College of Aerospace and Civil Engineering, Harbin Engineering University, Harbin 150001, PR China

(Received 18 April 2023; revised 3 November 2023; accepted 21 December 2023)

This study gives insights into the interfacial instabilities of a ventilation cavity by injecting gas vertically into the horizontal liquid crossflow through both numerical and experimental investigations. We identified four distinct regimes of the ventilation cavity based on their topological characteristics: (I) discrete bubble, (II) continuous cavity, (III) bifurcated cavity, and (IV) bubble plume. The boundaries for these regimes are delineated within the parameter space of crossflow velocity and jet speed. A comprehensive analysis of the flow characteristics associated with each regime is presented, encompassing the phase mixing properties, the dominant frequency of pulsation, and the time-averaged profile of the cavity. This study conducted a detailed investigation of the periodic pulsation at the leading-edge interface of the cavity, also known as the 'puffing phenomenon'. The results of local spectral analysis and dynamic mode decomposition indicate that the high-frequency instability in the near-field region exhibits the most significant growth rate. In contrast, the low-frequency mode with the largest amplitude spans a broader region from the orifice to the cavity branches. A conceptual model has been proposed to elucidate the mechanism behind the pulsation phenomenon observed along the cavity interface: the pulsation results from the alternate intrusion of the crossflow and the cavity recovery at the leading edge, being governed mainly by the periodic oscillating imbalance between the static pressure of gas near the orifice and the stagnation pressure of crossflow at the leading edge.

Key words: cavitation, gas/liquid flows

† Email address for correspondence: zhangaman@hrbeu.edu.cn

1. Introduction

The interaction between a transverse jet through an orifice and an orthogonal incoming flow, also known as jet in crossflow (JICF) has been investigated extensively due to its relevance to diverse engineering applications, such as fluid mixing in combustion (Gruber *et al.* 1997; Schlüter & Schönfeld 2000; Chai, Iyer & Mahesh 2015), film cooling (Acharya, Tyagi & Hoda 2001; Peterson & Plesniak 2004), drag reduction (Elbing *et al.* 2013; Mäkiharju *et al.* 2017; Gan *et al.* 2022) and pollutant dispersal (Saïd *et al.* 2005; Arora & Saha 2011). A thorough literature review on single-phase JICF problems can be found in Mahesh (2013). However, multiphase JICFs exhibit even more complex hydrodynamic features and interfacial phenomena due to the different phases of the crossflow and the jet (Marshall 1992; Lee 2015; Broumand, Birouk & Mahmoodi 2019). In the present study, our emphasis lies in understanding the instability in the ventilation cavity and the mechanisms triggering such instabilities from gaseous injections into a liquid crossflow.

It has been a consensus that the canonical single-phase JICF exhibits flow structures such as the jet shear-layer vortex, the horseshoe vortex, the wake vortex, the counter-rotating vortex pair (CVP), and the hairpin vortex. These flow structures have been categorized based on their morphology, spatial distribution and formation mechanisms (Fric & Roshko 1994; Kelso, Lim & Perry 1996; Cortelezzi & Karagozian 2001; Mahesh 2013). The shear-layer vortex, which wraps around the jet interface and extends from the orifice, is attributed to the Kelvin–Helmholtz instability. This instability grows autonomously along the interface, driven by the pronounced shear gradient. The formation of the horseshoe vortex upstream of the jet arises from the unfavourable pressure gradient in the local crossflow and the separation of the near-wall boundary layer. While the wake vortices trailing the jet bear resemblance to those behind a cylinder, their formation mechanisms are fundamentally distinct. The vorticity in the former originates from the wall boundary layer, in contrast to the latter, which stems from the shear flow wrapping around the cylinder. The CVP is the largest structure in the time-averaged flow of JICF. It originates from the near-field region of the orifice, and extends to the far end of the deflected jet. Although there is still some contradiction regarding the generation mechanism of the CVP among different literatures, the present study is not going to cover this issue, given the limited relevance of the CVP in the context of multiphase JICF. Finally, the train of hairpin vortices forms predominantly at low-velocity ratios $r = U_j/U_\infty < 1$. In this context, U_j denotes the mean jet velocity, and U_∞ denotes the speed of the crossflow. This scenario is similar to the bypass transition of a plane boundary layer subjected to intensive external disturbances.

The linear stability analyses (Alves, Kelly & Karagozian 2008; Bagheri *et al.* 2009; Ilak *et al.* 2012; Peplinski, Schlatter & Henningson 2015; Regan & Mahesh 2019) and mode decomposition analyses (Regan & Mahesh 2017; Gevorkyan *et al.* 2018; Shoji *et al.* 2020; Schmid 2022) have been employed to shed more light on the flow instabilities resulting in the emergence of unsteady vortex structures of single-phase JICF. It has been identified that the high-frequency unstable global eigenmodes are associated with the shear-layer instabilities, and the low-frequency ones are related to the wake vortices (Bagheri *et al.* 2009). With increasing velocity ratio, Ilak *et al.* (2012) identified the appearance of the first unstable eigenmode at $r = 0.675$. This instability constitutes the origin of the hairpin vortices shedding from the jet shear layer. Furthermore, Peplinski *et al.* (2015) employed non-modal linear analyses to investigate the transient effect, and determined that the critical value of r corresponding to the optimal initial perturbation lies in the range between 1.5 and 1.6. It was found that the series of backward-tilting waves at the base of a CVP result in the most significant transient growth.

Through proper orthogonal decomposition (POD) of the instantaneous velocity fields measured experimentally by particle image velocimetry (PIV), Meyer, Pedersen & Özcan (2007) identified that the shear-layer vortices are the leading unstable modes at low velocity ratios, while the wake vortices prevail at high velocity ratios. Regan & Mahesh (2017) highlighted that the eigenmodes derived from the dynamic mode decomposition (DMD) of the direct numerical simulations share similarities in spatial distribution and primary frequencies with those from linear stability analyses. They also demonstrated that the dominant instability transforms from the upstream shear layer at $r = 2$ to the downstream shear layer of the jet at $r = 4$. In a comparison between the DMD and POD modes derived from identical JICFs, Rowley *et al.* (2009) suggested that DMD modes possess superior capability over POD modes in discerning the fundamental unsteady dynamics from such complex nonlinear flows. This distinction arises as each DMD mode aligns with a singular frequency component, in contrast to the POD modes, which are modulated by time coefficient sequences encompassing various frequency components.

Buoyancy plays an important role in the modulation of flow structures due to the significant difference in density between the fluid mediums in multiphase JICFs. Therefore, the flow dynamics in multiphase JICFs notably deviate from single-phase JICFs, and the Froude number must be considered to characterize the effect of gravity. The formation of a ventilation cavity or bubble by a gas jet in a liquid crossflow manifests unique flow patterns because of mass and momentum transfers across phase boundaries. Specifically, the immediate generation of discrete bubbles at the orifice was observed in situations with a low Froude number and reduced gas flow rates (Wace, Morrell & Woodrow 1987; Marshall 1992). Mirsandi *et al.* (2020) suggested that the detachment of a single bubble from the orifice is governed by the combined effects of surface tension, buoyancy and drag forces. In contrast, the formation of a bubble plume is observed under conditions where the Froude number and gas flow rate are significantly high. As a result, the horizontal motion of the crossflow overcomes the restoring force of the liquid, leading to the dispersion of the foamy flow at a certain distance from the orifice and forming a bubble plume (Socolofsky & Adams 2002; Dong *et al.* 2020). Neither scenario above favours drag reduction, since the optimal condition demands a continuous cavity or layer of gas covering the underwater surface of marine vehicles (Ceccio 2010). Silberman & Song (1961) investigated experimentally the development of the ventilation cavity in a vertical water tunnel, and revealed that a stable cavity could be produced only when the ventilation cavitation number exceeded a critical value. Using a similar experimental set-up, Vigneau *et al.* (2001) suggested that the thickness of the boundary layer does not have any significant influence on the dynamics of the cavity. Additionally, they verified the non-existence of CVP within the cavity formed from injecting gas horizontally into a vertical liquid crossflow.

The practical utilization of air layer drag reduction (ALDR) has raised attention considerably on downward gas injection beneath a flat surface through an orifice or slot (Hakki, Insel & Helvacioglu 2010; Elbing *et al.* 2013; Mäkiharju *et al.* 2017; Mäkiharju & Ceccio 2018; Wang *et al.* 2020). Previous studies have shown a significant interest in the distinct flow characteristics of ventilation cavities, particularly the bifurcation of the cavity into dual branches. Between the gaseous branches, the filling fluid can be purely liquid (Λ-type) or a thin sheet of air layer (Δ-type), depending primarily on the Froude number and the dimensionless ventilation rate. According to Mäkiharju *et al.* (2017), the action of buoyancy drives the gas towards the wall and splits the cavity into distinct branches. They also established a scaling law to predict the variation of other topology characteristics of the cavity, including the branch sweep angle and the chord length, based on the Froude

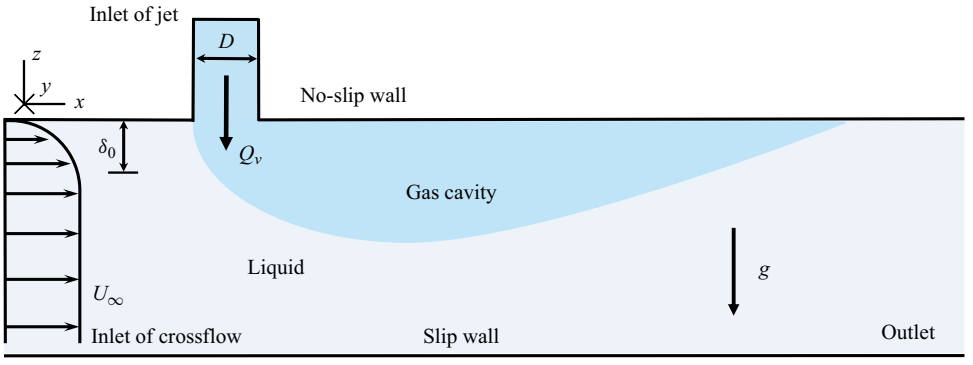

Figure 1. Schematic diagram of the computational set-ups in the near field, with a no-slip top wall, slip bottom wall, inlet and outlet boundary for crossflow, and the inlet for gas injection. Here, Q_v and D represent the gas volume flow rate and the orifice diameter of the injector, respectively, and U_∞ and δ_0 denote the free-stream velocity and boundary layer thickness at the inlet, respectively. The boundary layer thickness at the inlet, δ_0, is defined as the vertical displacement between the top wall and the position where the local streamwise velocity satisfies $u = 0.99U_\infty$. The size of the computational domain is $L_x \times L_y \times L_z = 1.2\ \text{m} \times 1.0\ \text{m} \times 0.5\ \text{m}$.

number $F_r = U_\infty/\sqrt{g\delta_0}$, the Reynolds number of the crossflow $Re_\infty = U_\infty\delta_0/\nu_\infty$, the scaled ventilation rate, $Q^* = Q_v/U_\infty\delta_0^2$, and the velocity ratio, $r = U_j/U_\infty$. Mäkiharju & Ceccio (2018) extended the study from a single orifice to multi-point holes of gas injection, and investigated the interaction between adjacent cavities. They found that the formation of stable and continuous air layers is possible only under the appropriate distribution of holes and the ventilation rate. Wang *et al.* (2020) compared the morphology, closure patterns and shedding features of ventilation cavities with diverse experimental set-ups, including air injection methods via slot or holes, and facilities of water tunnels or towing tanks. They proposed that the cavity by gas injection from multi-point holes tends to approach asymptotically that from a slot with the increasing number and closer spacing of holes.

The aim of this study is to classify the flow regimes resulting from the downward injection of gas into a liquid crossflow under diverse conditions, and to uncover the mechanisms triggering interface instabilities. The rest of the paper is organized as follows. The numerical models and experimental set-ups are introduced in § 2, while the detailed validation tests are presented in an Appendix. The classification of cavity typologies and the related flow characteristics are discussed in § 3. The mechanisms responsible for the cavity instabilities are investigated in § 4. Concluding remarks are presented in § 5.

2. Methodology

2.1. *Numerical model*

The schematic diagram presented in figure 1 illustrates the numerical model employed in the simulations. A reference frame is set up with its axes x, y, z corresponding to the streamwise, spanwise and wall-normal directions, respectively. The upper boundary consists of a no-slip wall and an orifice of a circular injection pipe with diameter D and length L_p. The centre of this orifice serves as the origin of the reference frame. The boundary layer with thickness δ_0 is assigned on the inlet boundary. Unless stated otherwise, the velocity profile of the boundary layer follows a 1/7 power law given by $U(z) = U_\infty(z/\delta_0)^{1/7}$. The gas is injected into the pipe with mean velocity U_j at the inlet

Case	D (mm)	U_∞ (m s^{-1})	U_j (m s^{-1})	δ_0 (mm)	J	Re_∞	Re_j	Fr
1	10	3.00	63.70	50	0.54	1.50×10^5	4.24×10^4	4.29
2	10	3.00	30.00	50	0.12	1.50×10^5	2.00×10^4	4.29
3	5	3.00	254.80	50	8.65	1.50×10^5	8.49×10^4	4.29
4	1	0.75	4.00	50	0.03	3.75×10^4	2.67×10^2	1.07
5	1	3.00	63.70	50	0.54	1.50×10^5	4.25×10^3	4.29
6	2	3.00	63.70	50	0.54	1.50×10^5	8.49×10^3	4.29
7	5	3.00	63.70	50	0.54	1.50×10^5	2.12×10^4	4.29
8	1	0.75	4.00	3	0.03	2.25×10^3	2.67×10^2	4.37
9	5	3.00	254.80	6	8.65	1.80×10^4	2.12×10^4	12.37
10	10	3.00	127.40	50	2.16	1.50×10^5	8.49×10^4	4.29
11	10	3.00	191.10	50	4.87	1.50×10^5	1.27×10^5	4.29

Table 1. Physical conditions and dimensionless parameters of each case in the present numerical simulations.

of the pipe. A free slip condition is applied on the bottom boundary, and the outlet is prescribed by a Neumann velocity boundary condition and a Dirichlet pressure boundary condition, taking into account the static pressure distribution induced by gravity.

Table 1 summarizes the flow conditions of 11 numerical cases presented in this paper, which investigate the influence of the pipe diameter D, the crossflow velocity U_∞, the jet flow velocity U_j, and the boundary layer thickness δ_0. The variation of physical flow conditions leads to the corresponding changes in the dimensionless parameters, namely the momentum flux ratio $J = \rho_j U_j^2/(\rho_\infty U_\infty^2)$, Reynolds numbers of the crossflow, $Re_\infty = U_\infty \delta_0/\nu_\infty$, and the jet flow, $Re_j = U_j D/\nu_j$, and Froude number Fr. The densities of gas and liquid are $\rho_j = 1.2$ kg m^{-3} and $\rho_\infty = 1.0 \times 10^3$ kg m^{-3}, respectively. Additionally, the kinematic viscosities for gas and liquid, $\nu_j = 1.5 \times 10^{-5}$ m^2 s^{-1} and $\nu_\infty = 1.0 \times 10^{-6}$ m^2 s^{-1}, are employed in the simulations. The surface tension coefficient is taken as $\sigma = 0.07$ N m^{-1}.

The numerical simulations were performed by using the commercial software STAR-CCM+, which utilizes built-in algorithms of the wall-adapting local eddy-viscosity model (Nicoud & Ducros 1999), the volume-of-fluid method (Hirt & Nichols 1981), and the adaptive mesh refinement (AMR) scheme of hexahedron element (Berger & Colella 1989) for high-fidelity modelling of complex multiphase flows within the framework of the finite volume method. The bounded central-differencing scheme and the first-order Euler implicit scheme are selected for spatial and temporal discretization. An iterative manner through the SIMPLE (semi-implicit method for pressure-linked equation) algorithm (Patankar & Spalding 1972) is adopted to solve the continuity equation and the incompressible Naiver–Stokes equations:

$$\frac{\partial \rho}{\partial t} + \nabla \cdot (\rho \tilde{\boldsymbol{u}}) = 0, \tag{2.1}$$

$$\frac{\partial}{\partial t}(\rho \tilde{\boldsymbol{u}}) + \nabla \cdot (\rho \tilde{\boldsymbol{u}} \otimes \tilde{\boldsymbol{u}}) = -\nabla \cdot \tilde{\boldsymbol{p}} \boldsymbol{I} + \nabla \cdot (\tilde{\boldsymbol{T}} + \boldsymbol{T}_{SGS}) + \rho \boldsymbol{g} + \sigma \kappa \nabla \alpha, \tag{2.2}$$

where the tilde signifies the filtered quantities with respect to the subgrid scale, and the fluid properties depend on the volume fraction of liquid α, such as $\rho = \alpha \rho_\infty + (1 - \alpha)\rho_j$ and $\mu = \alpha \mu_\infty + (1 - \alpha)\mu_j$. In addition, the viscous stress tensors $\tilde{\boldsymbol{T}}$ and $\boldsymbol{T}_{SGS}$ result from the resolved and unresolved eddies, respectively. The last term denotes the contribution by

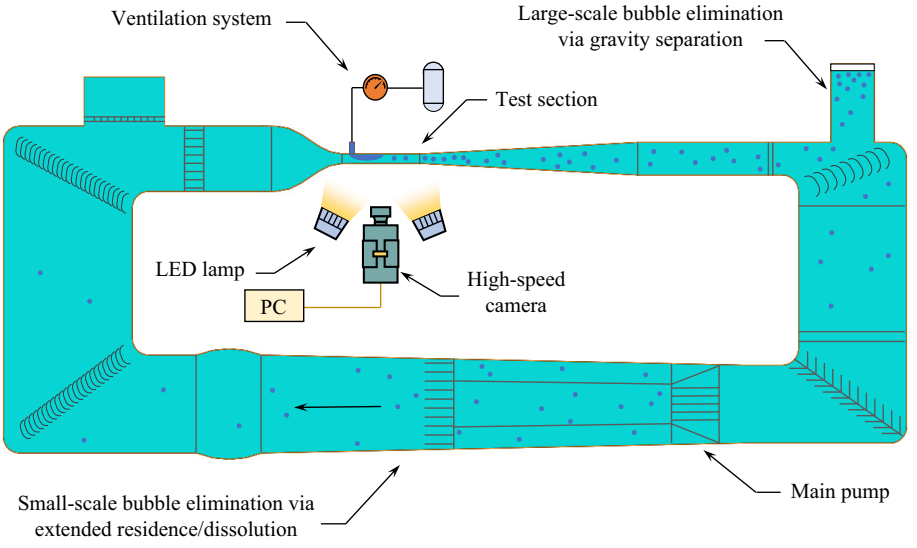

Figure 2. Schematic diagram of the experimental set-ups.

surface tension, where the curvature of the interface between two phases can be obtained by $\kappa = -\nabla \cdot (\nabla\alpha/|\nabla\alpha|)$. Finally, the phase transport is determined by the advection equation:

$$\frac{\partial \alpha}{\partial t} + \tilde{\boldsymbol{u}} \cdot \nabla\alpha = 0. \tag{2.3}$$

The dimensions of the computational domain are $L_x \times L_y \times L_z = 1.2\ \text{m} \times 1.0\ \text{m} \times 0.5\ \text{m}$. With reference to Mäkiharju *et al.* (2017), who investigated two-phase JICF numerically and experimentally under comparable momentum flux ratios, the domain size is considered sufficient for the complete development of the cavity flow. The ventilation pipe, with length $L_p = 2D$, is located 0.2 m downstream from the inlet boundary of the crossflow, where the velocity profile of the boundary layer with the thickness δ_0 is specified at the inlet. The characteristic length $D_0 = 10\ \text{mm}$ is used to normalize the spatial coordinates. Preliminary mesh refinement is applied to the no-slip wall, particularly the region inside the pipe and near the orifice. Additionally, AMR is activated around the gas–liquid interface to capture accurately the morphology of the cavity. A comprehensive validation of the present numerical model is presented in the Appendix, which demonstrates that a minimum cell size $\Delta x_{min} = 0.1D$ and Courant number $C_r = U_j \Delta t/\Delta x_{min} < 1$ are sufficient to obtain accurate and convergent results.

2.2. *Experimental facilities and methods*

The experiments were conducted in a cavitation water tunnel equipped with a ventilation system, as shown in figure 2. The test section has overall dimensions 600 mm length and square cross-section 100 mm × 100 mm. All tests were carried out at normal temperatures ($\approx 20\,^{\circ}\text{C}$) and atmospheric pressure ($\approx 10^5$ Pa). As a result, the density and viscosity of fluids in experiments are approximately identical to the values adopted in the numerical counterparts. The degassing system was also included in the tunnel to mitigate the influence of previously injected bubbles on the test section. The ventilation system consists of an air compressor, a pressure tank, a digital flow-rate gauge and a switchable gas

D (mm)	U_∞ (m s^{-1})	U_j (m s^{-1})	J	Re_∞	Re_j
1	0.5–4.0	4–418	0.08–839	1.50×10^3–2.40×10^4	2.67×10^2–2.79×10^4
2	0.5–4.0	4–397	0.08–839	1.50×10^3–2.40×10^4	5.33×10^2–5.29×10^4

Table 2. Physical and dimensionless parameters of experimental tests.

injection pipe with a contraction section. Compared to the towed model in a water basin at rest employed by Mäkiharju *et al.* (2017), the boundary restriction of our limited test section would be terribly prominent for their injection pipes with diameters $D = 5$, 10 and 20 mm. Therefore, the present study adopted $D = 1$ and 2 mm for the experimental tests, while the effect of D on flow regimes and characteristics will be investigated both experimentally and numerically.

The cavity morphology was captured from both the side and top views using a high-speed camera (Photron AX200) equipped with a Tokina 100 mm F2.8 lens at rate 6000 frames per second and resolution 1024×672 pixels. Back-lighting and front-lighting LED illumination modules were positioned for optimal clarity in capturing the side and top views of the cavity morphology, respectively. To facilitate the comparison between the numerical and experimental results, the crossflow velocity U_∞ was varied between 0.5 m s^{-1} and 4 m s^{-1}, and the jet velocity U_j ranged from 4 m s^{-1} to 418 m s^{-1}. Table 2 lists the variation range of dimensionless parameters associated with all experimental tests in the present study.

In addition, the velocity profiles of the boundary layer upstream to the orifice were obtained by PIV. The mean diameter of the particles used in our experiments is approximately 13 nm, corresponding to a Stokes number within the range $O(10^{-2})$ to $O(10^{-3})$. Therefore, the seeding particles are considered to reflect the fluid motion, with an error below 1 % (Pescini *et al.* 2015). The green laser with 532 nm wavelength generated by Beamtech EMER-532-20 is introduced from the bottom side of the test section of the water tunnel to illuminate the particles flowing over the centre x–z plane. We utilized the multi-pass cross-correlation approach with fast Fourier transform window deformation built in PIVlab 2.5.4 (Thielicke & Stamhuis 2014). Four interrogation window sizes, namely 64×64 pixels, 32×32 pixels, and 16×16 pixels and 12×12 pixels with 50 % overlap, are used. Given the spatial resolution 0.03 mm pixel^{-1} from the image by the high-speed camera and the minimum analysis window, the velocity field can be resolved to 0.18 mm, enabling the precise delineation of the boundary layer profile.

3. Regimes of the ventilation cavity

This section delineates four distinct flow regimes of the ventilation cavity and three transitional regimes, distinguished by their topological and interfacial features, as summarized in table 3. Based on comprehensive experimental results, these flow regimes are categorized within the U_j–U_∞ parameter space. Furthermore, based on the numerical results, we present quantitative analyses concerning the mixing properties, time-averaged fields and oscillation frequency spectrum to deepen our understanding of cavity instabilities.

Abbreviation	Flow regime	Abbreviation	Flow regime
DB	Discrete bubbles	DB-TR	Transitional region between DB and CC
CC	Continuous cavity	CC-TR	Transitional region between CC and BC
BC	Bifurcated cavity	BC-TR	Transitional region between BC and BP
BP	Bubble plume		

Table 3. Abbreviations for four distinct flow regimes of the ventilation cavity and three transitional regimes.

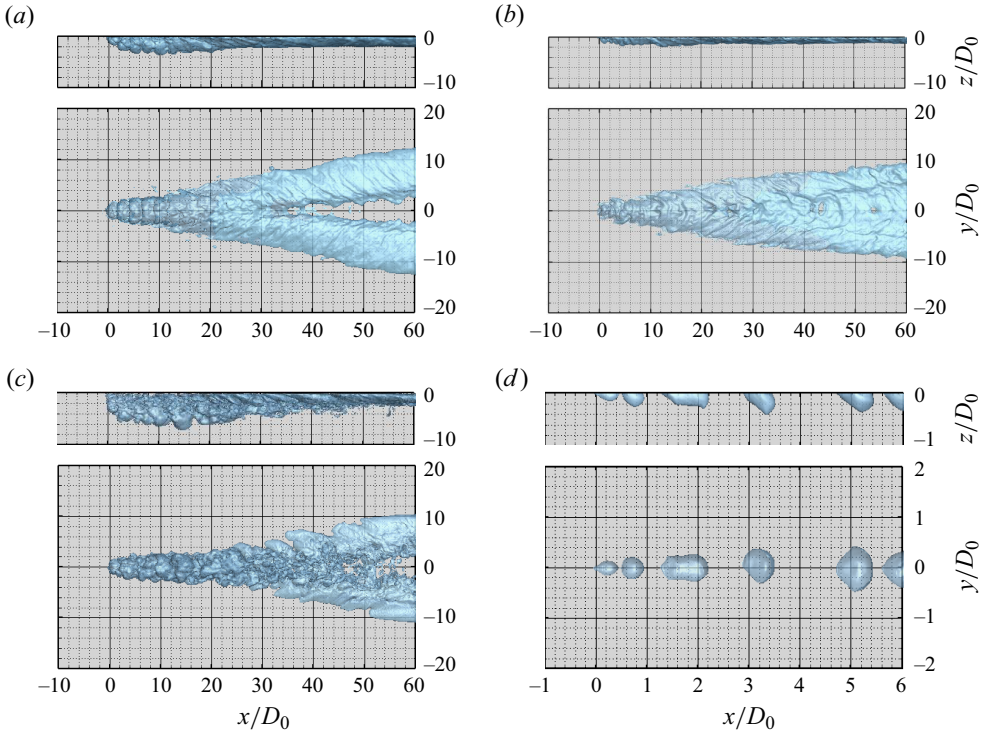

Figure 3. The typical instantaneous cavity topology in four regimes obtained by numerical simulations, from both the side and plan views: (*a*) bifurcated cavity (BC, case 1); (*b*) continuous cavity (CC, case 2); (*c*) bubble plume (BP, case 3); (*d*) discrete bubbles (DB, case 4).

3.1. *The regime classification*

As shown in figure 3, four distinct flow regimes are identified based on the interfacial characteristics of the ventilation cavity. The bifurcated cavity (BC) regime is distinguished by the division of the gas pocket into two separate branches, with little gas remaining between them. In contrast, the gas pocket generally remains intact in the continuous cavity (CC) regime. These two regimes align with Λ-type and Δ-type cavities, respectively, as described by Mäkiharju *et al.* (2017). Within the regime of bubble plume (BP), the interface of the gas jet undergoes significant deformation, eventually fragmenting into turbulent foamy bubbles. Buoyancy plays a relatively less important role in the BP regime, and the near-field phenomena of gas evolution resembles those of an inverted multiphase JICF (Dong *et al.* 2021). Finally, the semi-spherical cavities detach intermittently from

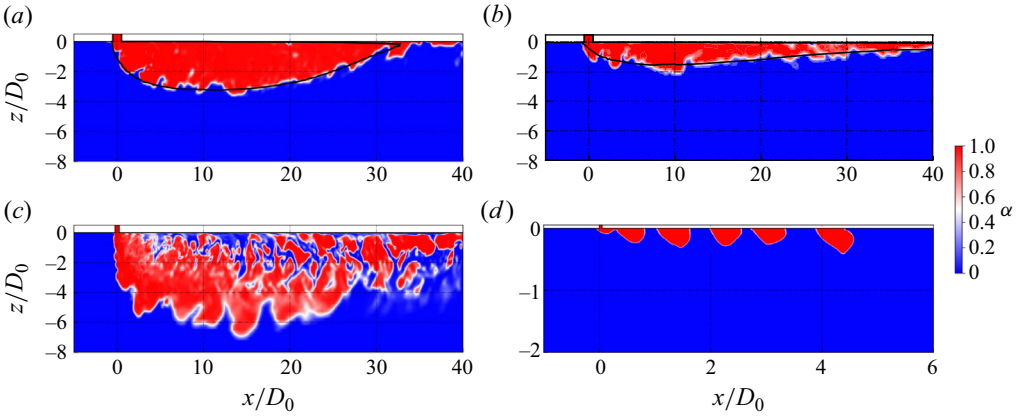

Figure 4. The distribution of gas volume fraction on the centre plane, corresponding to the four regimes (cases 1–4) shown in figure 3. The solid black curves indicate the time-averaged boundary of the cavity in the BC and CC regimes.

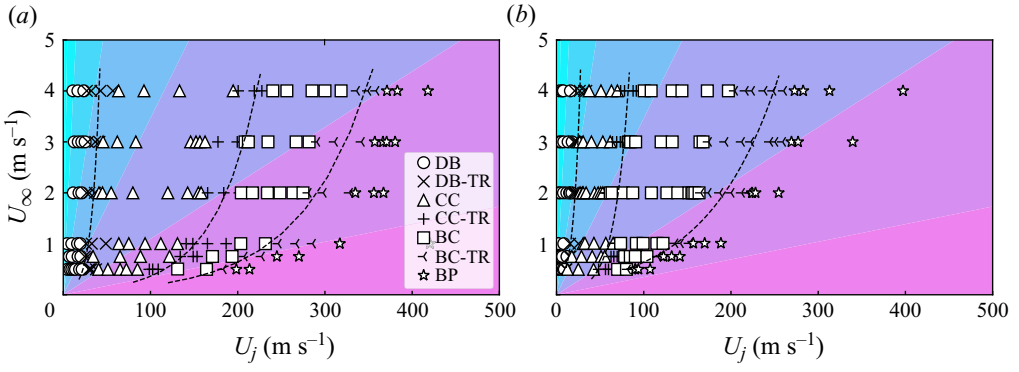

Figure 5. Classification of flow regimes of gaseous injection into liquid crossflow through experimental observations for the orifice diameters of (*a*) $D = 1$ mm and (*b*) $D = 2$ mm. Here, BD-TR, CC-TR and BC-TR represent the transitional statuses between the adjacent flow regimes.

the orifice, giving rise to a consistent sequence of discrete bubbles (DB) that traverse the boundary wall. This observation aligns with the scenario documented in Marshall (1992).

The interfacial features on the centre plane of the ventilation cavities across the various regimes are exhibited in figure 4. Even though the ventilation cavity demonstrates some instability in the BC and CC regimes, typically interfacial disturbances develop and propagate along the time-averaged boundaries of the cavity, as denoted by the solid black curves in figures 4(*a*,*b*). Comparatively, the gas pocket of the flow in the BC regime is thicker than that in the CC regime due to the increase of penetration depth for higher momentum flux ratio. The most prominent interfacial features of the BP regime, as shown in figure 4(*c*), are the entrainment of droplets inside the ventilation cavity and the scattering of bubbles resulting from the cavity's collapse at the leeward-side interface. Figure 4(*d*) indicates that the jet in the DB regime is pinched off from the neck at the near field downstream of the orifice, where the periodic bubble departure takes place.

Figure 5 maps out the flow regimes for $D = 1$ and 2 mm in U_∞–U_j space. The four flow regimes DB, CC, BC and BP appear successively, with the increase of jet rate for the

	DB-TR			CC-TR			BC-TR		
	A_1	A_2	R^2	A_1	A_2	R^2	A_1	A_2	R^2
1 mm	0.04	0.11	0.75	0.05	0.02	0.52	0.05	0.01	0.97
2 mm	0.13	0.13	0.91	0.03	0.06	0.64	0.19	0.01	0.67

Table 4. Coefficients of the fitted transitional curves with the functional expression $y = A_1\,\mathrm{e}^{A_2 x}$, as shown in figure 5. Here, R^2 denotes the coefficient of determination for these fitted curves.

crossflow velocity varying from 0.5 m s^{-1} to 4 m s^{-1}. The boundary curves are generally laid on the transitional regions, namely DB-TR, CC-TR and BC-TR, which is due to the supercritical nature of the regime transition of the ventilation cavity. The fitted curves have the exponential function form $y = A_1\,\mathrm{e}^{A_2 x}$. The data points used for the fitting curves are taken from the average of two limit points in each transitional regime, with the upper and lower jet velocity points for $U_\infty = 0.5$, 0.75, 1, 2, 3 and 4 m s^{-1}. Table 4 lists the coefficients for the fitted curves and their respective coefficients of determination for $D = 1$ and 2 mm. In the background of the regime map, the contour of the momentum flux ratio's logarithm, $\log(J)$, is depicted, spanning a range from -2 to 2 with interval increment 1. Typically, for $U_\infty < 1$, the flow regime is heavily influenced by J: the DB regime arises when $J < 0.1$, whereas the BP regime manifests solely for $J > 10$. At $U_\infty > 1$, the critical jet rate increases nonlinearly, leading to a progressive reduction in the J value defining the regime boundary. Despite the geometric similarity of the ventilation cavity of the same regime formed at different orifice diameters, the scaling relationships of the cavity topology are rather complex and may depend on multiple dimensionless parameters. A comparison between the regime distributions for $D = 1$ and $D = 2$ mm reveals that as the orifice size enlarges, the critical curves delineating flow transitions for CC-TR and BC-TR exhibit a pronounced leftward shift in U_∞–U_j space. For the regime boundaries with different orifice diameters, the exponent coefficients A_2 corresponding to the transition curves of DB-TR and BC-TR are similar. However, for the one corresponding to CC-TR, the exponent coefficient $A_2 = 0.06$ at $D = 2$ mm is significantly larger than $A_1 = 0.02$ at $D = 1$ mm, leading to a larger parameter range of the BC regime and a narrower one of the CC regime. The reason for this discrepancy might be that although the two-phase JICFs with different sizes of orifice are geometrically similar, buoyancy plays a more pronounced role in the larger-scale flow, leading to the earlier appearance of a bifurcating cavity. Although the scaling law proposed by Mäkiharju *et al.* (2017) depicts the cavity features in the BC regime, an extended set of physical parameters must be evaluated to comprehend the effects of surface tension, particularly concerning bubble detachment and cavity disintegration in the DB and BP regimes, respectively. Therefore, the Weber number $We = \rho_\infty U_\infty^2 R/\gamma$ is introduced to evaluate the ratio between the inertial force and surface tension force, where R denotes the curvature radius, $R = 1/\kappa$. Hence surface tension plays primarily a significant role in small-scale and low-velocity flows, dominating the formation of bubbles and droplets in multiphase JICFs.

The transition of flow regimes with increasing the jet rate for $U_\infty = 0.75$, 2 and 3 m s^{-1} is exhibited in figure 6. It is clear that the ventilation cavity in transitional flow regimes manifests an intermediate state between the adjacent typical regimes. In the DB-TR regime, the pulsation near the orifice is analogous to that of the CC regime, but the gas pocket gets pinched off intermittently, forming discrete cavities downstream. Unlike flow in the typical BC regime, the bifurcation of the cavity in the CC-TR regime

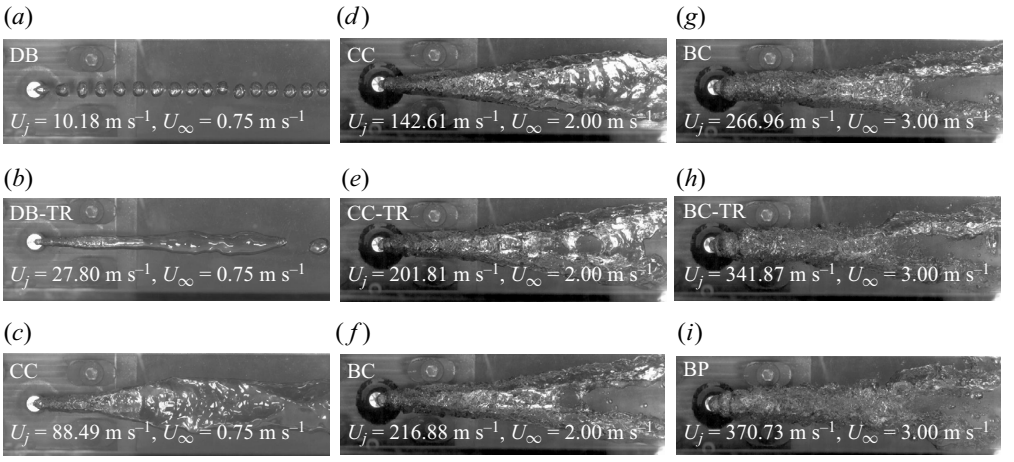

Figure 6. A comparison of the instantaneous cavity morphologies between the typical regimes and transitional regimes through experimental observations for $D = 1$ mm.

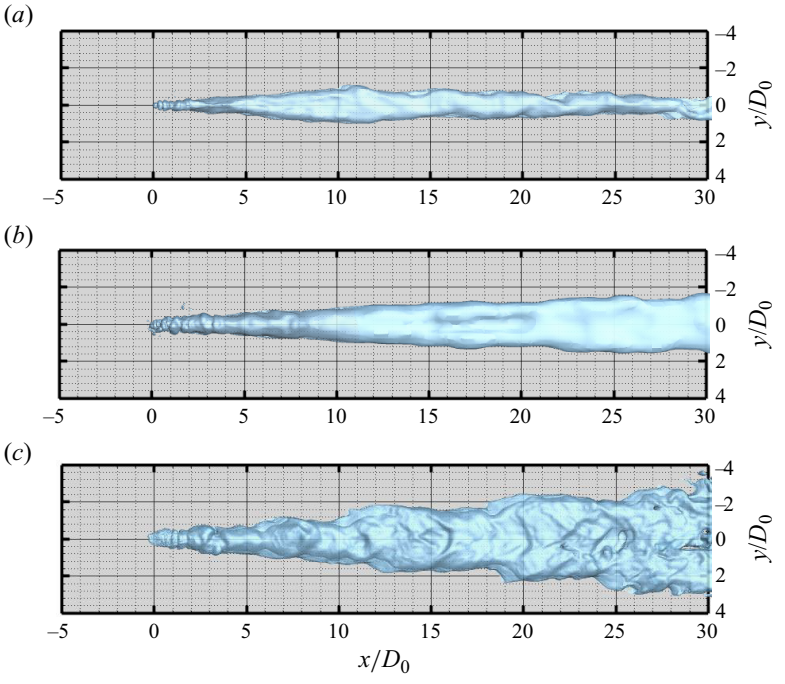

Figure 7. A comparison of the instantaneous cavity morphologies of the numerical simulations with the same momentum flux ratio $J = 0.54$ but different orifice diameters: (*a*) $D = 1$ mm, case 5; (*b*) $D = 2$ mm, case 6; and (*c*) $D = 5$ mm, case 7.

occurs intermittently at fairly unpredictable locations. Finally, in the BC-TR regime, the unsteadiness of the cavity interface results in the separation of small-scale bubbles near the orifice. However, the integrity of the interface is recovered on the downstream branches. Additionally, the influence of the orifice diameter on the cavity topology is investigated by comparing the cavity typologies of the cases with the same momentum flux ratio. As indicated in figures 7 and 3(*a*), the cavity regime undergoes a transition from

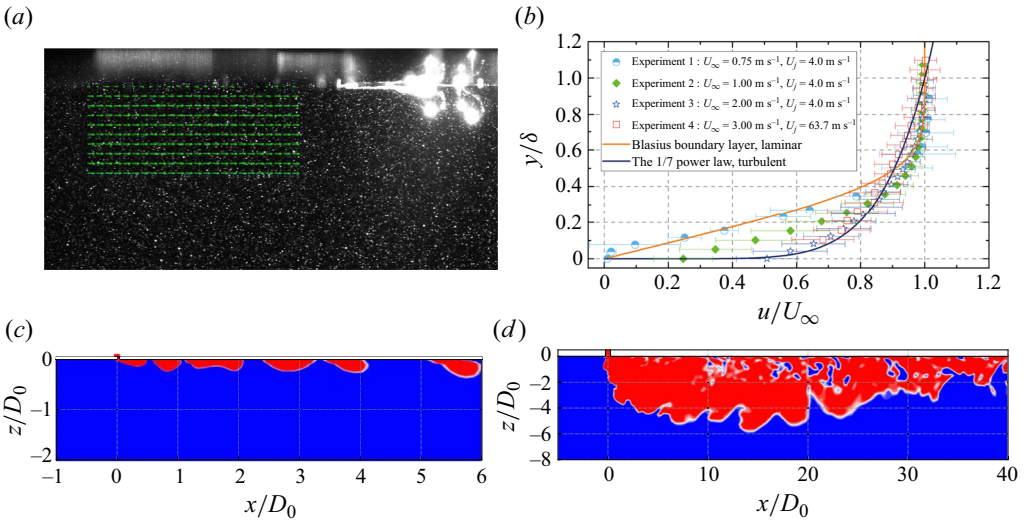

Figure 8. Boundary layer profiles upstream to the orifice obtained from PIV results and their influence on cavity evolution. (*a*) Snapshot of the velocity vector field at $(U_\infty, U_j) = (0.75\ \text{m s}^{-1}, 4.0\ \text{m s}^{-1})$. (*b*) Time-averaged velocity profile of boundary layer normalized to facilitate comparison with analytical solutions, with the boundary layer thickness $\delta_0 \approx 3.0$, 3.2, 4.9 and 6.0 mm, corresponding to Experiments 1–4, respectively. Numerical results of (*c*) case 8 and (*d*) case 9, as detailed in table 1, where the exact velocity profiles extracted from the PIV test were employed as inlet boundary condition.

DB-TR ($D = 1$ mm) to CC ($D = 2$ mm), then to CC-TR ($D = 5$ mm), and finally to BC ($D = 10$ mm), with the increasing sweep angle. The above observations demonstrate that the scale effect has a significant influence on the flow regimes of the ventilation cavity. Increasing the characteristic length, i.e. the orifice diameter, not only changes the time-averaged shape of the cavity but also affects the evolution of interfacial instabilities. The scale effects of multiphase JICFs can be attributed primarily to the following three reasons: (i) an increase in the jet Reynolds number, leading to enhanced turbulence and more intense phase mixing at the interface; (ii) an increase in the Weber number, weakening the effect of surface tension and diminishing the formation of discrete bubbles; and (iii) a reduction in the Froude number, amplifying the role of buoyancy, resulting in a flatter cavity interface and higher sweeping angle, facilitating the formation of bifurcations in the ventilation cavity influenced by buoyancy.

The influence of the crossflow boundary layer upstream to the orifice upon the cavity evolution is examined further. As depicted in figure 8(*a*), the PIV system measures the actual velocity field of the inlet boundary layer upstream of the orifice. Figure 8(*b*) indicates that the laminar flow persists at $U_\infty = 0.75$ m s^{-1} for consistency with the Blasius velocity profile. On the other hand, the velocity profile at $U_\infty = 3$ m s^{-1} aligns with the analytical solution from the 1/7 power law, suggesting the fully turbulent state. The velocity distributions at $U_\infty = 1$ and 2 m s^{-1} are scattered between two analytical curves, indicating a transitional state between laminar and turbulent flow. Therefore, the boundary layer thickness is deduced to vary around 5 mm in the present experimental tests. To analyse further the boundary layer thickness on cavity evolution, the mean velocity profiles obtained from the counterpart conditions of cases 8 and 9 were employed on the inlet boundary for comparison with cases 4 and 3, respectively. By comparing figures 4(*d*)

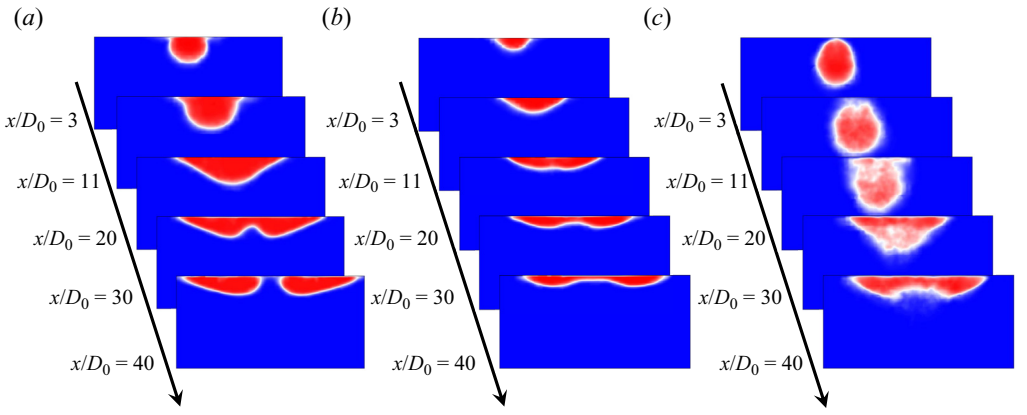

Figure 9. The time-averaged contours of the cavity along the streamwise direction obtained from the numerical simulations: (*a*) case 1, BC; (*b*) case 2, CC; and (*c*) case 3, BP.

and 8(*c*), we found that the flow phenomena in the DB regime are generally less affected by δ_0. In contrast, a subtle transition from BP to BC regimes in the high-J case is visible from a comparison between figures 4(*c*) and 8(*d*). This observed change can be attributed to the alterations in the flux ratio of crossflow to gas injection, influenced by the velocity profile at the leading edge of the orifice. This flux ratio is decreased with increasing boundary layer thickness, resulting in a strong gas penetration and more entrainment of droplets into the lee side of the jet, as observed in the BP regime.

3.2. *The regime characteristics*

The flow characteristics of the ventilation cavity in typical regimes are analysed further below. Figure 9 displays the time-averaged distributions of gas volume fraction at a series of cross-sections along the streamwise direction. In the BC regime, the cavity section initially forms a semicircular shape near the orifice at $x/D_0 = 3$. Starting from $x/D_0 = 11$, the interface curve deforms gradually from a parabolic style to a shape resembling a 'W', which develops a central hollow and eventually bifurcates into two branches at $x/D_0 = 30$. The development of the cavity in the CC regime generally resembles that in the BC regime but with a thinner air layer. Despite the concave interface at the centre, the cavity remains connected. In the BP regime, the cross-section formed a complete circle at $x/D_0 = 3$, resulting from the jet detached from the wall under the high momentum flux ratio. Following the dissipation of energy and the dispersion of the bubble plume, buoyancy drives the cavity closer to the wall, and the interface becomes relatively vague at $x/D_0 > 20$.

The characteristics of two-phase mixing across various regimes hold significant relevance for engineering applications of ALDR. As such, we propose a non-dimensional quantification metric $C_g/\sqrt{S_g}$ to gauge the extent of mixing, where S_g represents the sectional area of the cavity, and C_g signifies the interfacial perimeter of the cavity on the corresponding streamwise slice. The quantification of the mixing extent is a non-dimensional parameter that ensures geometrical similarity invariance. As depicted in figure 10, case 3 (BP regime) exhibits a markedly enhanced two-phase mixing extent compared to the others, attributable to pronounced interfacial instability near the orifice and the emergence of foamy bubbles. On the other hand, the mixing property of case 1 (BC regime) and case 2 (CC regime) share a similar variation trend, but the former exhibits

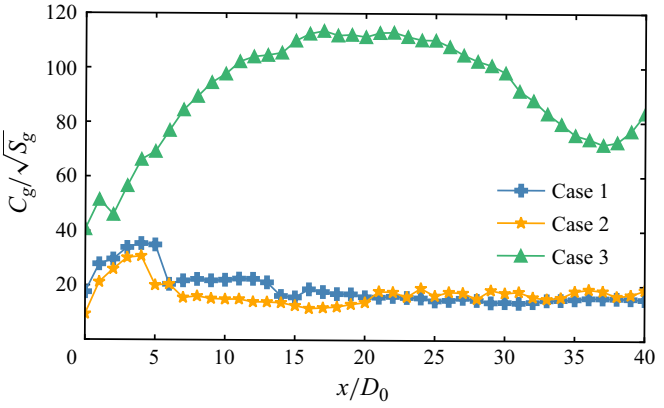

Figure 10. The quantification of the two-phase mixing extent along the streamwise direction based on the numerical results of cases 1–3, where S_g and C_g denote the area and the interfacial perimeter of the cavity on the streamwise cross-section, respectively.

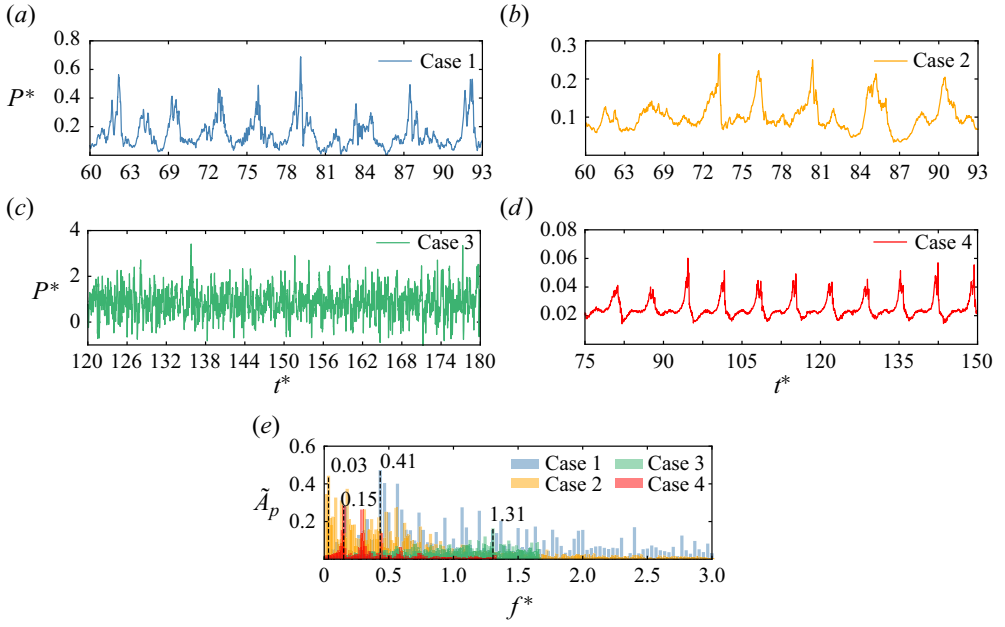

Figure 11. (*a*)–(*d*) Time history of the gas pressure at the jet inlet of the numerical results of cases 1–4, where the horizontal and vertical axes have been normalized by $t^* = tU_\infty/D$ and $p^* = p/(\rho_\infty U_\infty^2)$. (*e*) The spectral diagrams of normalized frequency of jet inlet pressure $f^* = fD/u_\infty$, where the amplitude has been normalized by $\tilde{A}_p = (A_p - \bar{P})/\sigma$. Here, $\bar{P}$ denotes the time-averaged pressure and σ denotes the standard deviation. The dashed line marks the dominant frequency of the largest amplitude for each case.

slightly greater values than the latter at $x/D_0 < 20$ because of the relatively stronger pulsation on the leading-edge cavity interface, which is pronounced near the orifice and then became attenuated downstream.

Figures 11(*a–d*) compare the trajectories of pressure pulsation at the injector for cases 1–4. For case 1, the instantaneous pressure exhibits strong periodicity, which

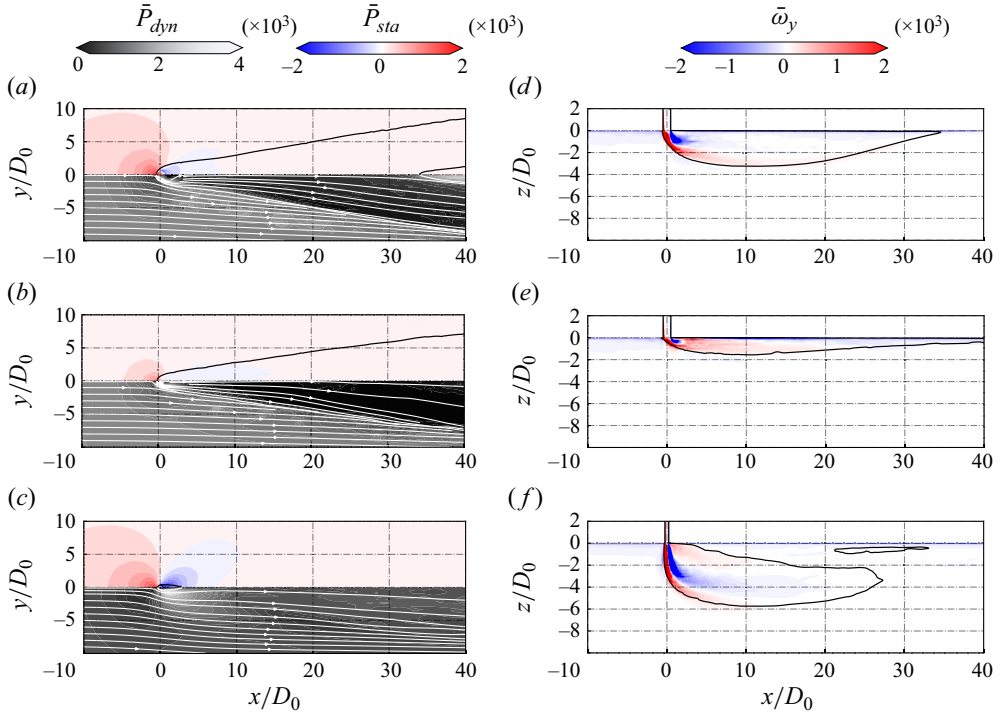

Figure 12. (*a–c*) Comparison of the time-averaged distribution of static pressure $\bar{P}_{sta}$ (upper side) and the planar dynamic pressure $\bar{P}_{dyn}$ (lower side) at the slice $z/D_0 = -0.3$ for cases 1–3. The mean cavity interface and streamlines are also denoted by the black and white solid lines. (*d–f*) The corresponding contours of mean spanwise vorticity $\bar{\omega}_y$ along with the cavity interface at the slice $y/D_0 = 0$.

corresponds to the regular puffing phenomenon at the near-field cavity surface. The relatively lower magnitude and dominant frequency of the pressure pulsation for case 2 indicate higher stability of the cavity interface in the CC regime compared to that in the BC regime. In contrast, intensive and rapid fluctuations of pressure are observed in case 3, and the scattered frequency spectrum shown in figure 11(*e*) suggests that there is no distinct dominant frequency in the BP regime. Finally, the intermittent sequential creation and detachment of individual bubbles led to regular and mild pressure oscillation, even though they exhibit the smallest amplitude among the discussed cases.

The distributions of time-averaged planar dynamic pressure and static pressure surrounding the cavity interface close to the upper wall are presented in figures 12(*a–c*). Across these three cases, a high static pressure region is apparent upstream of the orifice, whereas a low static pressure is observed on the cavity's leeward side. This characteristic flow pattern is akin to that of flow around a bluff body, as the vertical jet originating from the orifice hinders the crossflow and creates an adverse pressure gradient, which is especially obvious for case 3 due to the deep penetration depth of the jet. The distribution of planar dynamic pressure, which is obtained by $\bar{P}_{dyn} = 0.5\rho(u_x^2 + u_y^2)$, indicates the strength of flow parallel with the x–y plane. Within the ventilation cavity, the planar dynamic pressure of case 2 surpasses that of the other cases owing to the deflection of the jet velocity from the vertical direction under the intrusion effect of crossflow. As indicated in figure 12(*d*), the positive vorticity is exhibited at the leading edge, whereas negative vorticity appears on the leeward side of the orifice. In figure 12(*e*), the double-layer

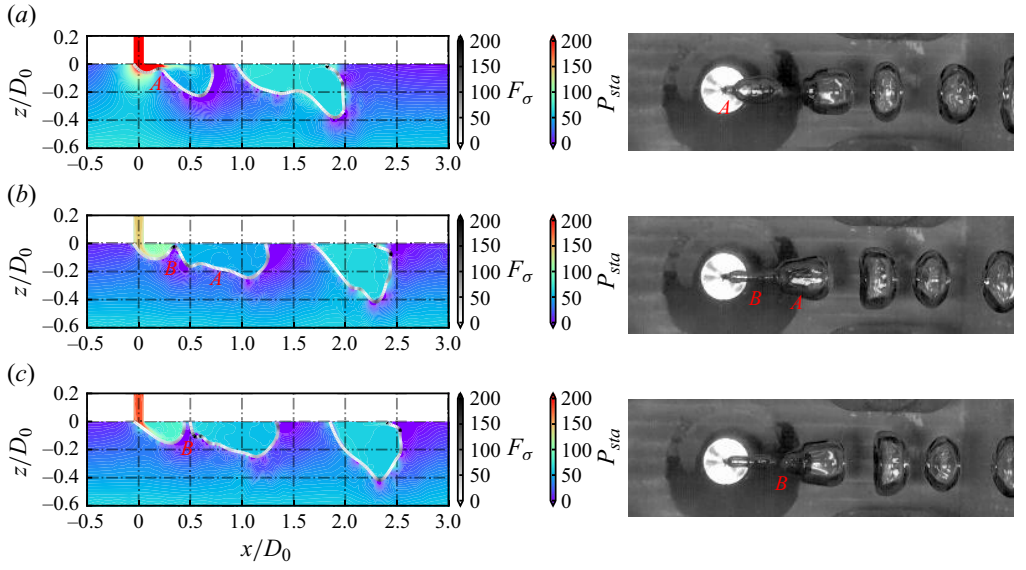

Figure 13. Instantaneous contours of static pressure inside the cavity P_{sta} for case 4 at tU_∞/D_0 values (*a*) 11.1, (*b*) 14.1 and (*c*) 14.7. The greyscale interface denotes the curvature on the bubble surface. The top views at the corresponding instants of bubble development from experimental observations are also shown on the right-hand side, whose animation is also provided in supplementary movie 1, available at https://doi.org/10.1017/jfm.2024.23.

structure is less discernible due to the milder shearing interaction between the crossflow and the jet in the CC regime. In addition to a higher amplitude of vorticity, figure 12(*f*) exhibits a triple-layer structure, which signifies the re-entrant flow on the leeward side. Besides presenting a heightened amplitude of vorticity, figure 12(*f*) exhibits a triple-layer configuration, indicative of the re-entrant flow on the leeward side.

The unique flow properties of multiphase JICF in the DB regime demand a dedicated discussion, considering the pivotal role of surface tension in the formation and disjunction of small-scale bubbles at low Weber numbers (Zhang *et al.* 2023). As depicted in figure 13(*a*), with corresponding animation provided in supplementary movie 1, the gas pocket started to grow at the first instant, when a noteworthy difference in static pressure can be observed between the two regions segregated by the neck at point *A*. As the interface curvature peaks at point *A*, surface tension exerts a force that tends to sever the bubble. Nevertheless, the high pressure inside the region near the orifice resisted this process, fostering the reinstatement of a smooth surface at this point (figure 13*b*). Simultaneously, the drag exerted by the crossflow results in the elongation of the bubble and the creation of a fresh interface indentation at point *B*. At this time, the internal pressure of the bubble fails to counterbalance the surface tension at point *B*, and the gas pocket eventually gets pinched off at the third instant present in figure 13(*c*). The separated bubble is transported swiftly downstream by the crossflow, engendering a succession of distinct bubbles as the above process repeats.

4. The flow instabilities of the bifurcated cavity

Due to the relevance to the practical application in ALDR, the flows in the BC regime have attracted a great deal of attention (Lee 2015; Choi, Lai & Lee 2016; Mäkiharju *et al.* 2017;

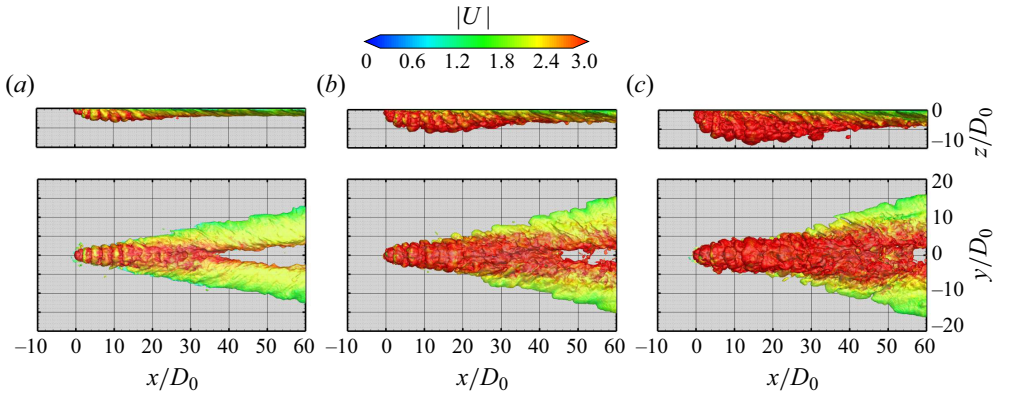

Figure 14. Instantaneous cavity interface of (*a*) case 1, (*b*) case 8 and (*c*) case 9, with the contour coloured by the magnitude of velocity.

Mäkiharju & Ceccio 2018). Although the flow instabilities of the bifurcated cavity are observed commonly in previous numerical and experimental studies, their characteristics and generation mechanisms have not been discussed comprehensively. In this section, we conduct qualitative and quantitative analyses on the near-field interface instability in the BC regime. The DMD has been utilized to identify the predominant patterns of interface fluctuation, and a theoretical model was introduced to elucidate the mechanisms precipitating interfacial instability and to account for the phenomenon of near-field puffing.

4.1. *The features of interface unsteadiness*

The flow structures of the ventilation cavity in the BC regime with varying Re_j, along with the velocity distribution on the interface, are displayed in figure 14. Similar to the results reported in Mäkiharju *et al.* (2017), the gas pocket near the orifice exhibits 'puffing' behaviour, namely the periodic oscillation and roll-up of the interface at the same frequency of pressure pulsation measured from the jet inlet. It is worth noting that the gas pocket retains a higher velocity magnitude on the central puffing interface than that of the branches. With an increase in the jet rate, the pocket acquires a longer and thicker puffing region with a loss in periodicity. Upon attaining maximal thickness, it began to split into two branches, where the minor wavy structures at the interface were discernible in both numerical and experimental findings of this study, as evidenced in figure 15 and the corresponding animation provided in supplementary movie 2, respectively.

Additional insights into the evolution of the cavity are elucidated in figure 16, which illustrates the propagation of the near-field instability across three cases within the BC regime. In addition to depicting the central interface at various moments, several Lagrangian points were monitored to provide a more comprehensive view of the cavity evolution. It is shown that the autonomous processes of near-field puffing consist of intrusion of crossflow at the leading edge and the downstream roll-up of the interface. The interfacial deformation is most pronounced at the position of maximum thickness, and then is moderate at the closure of the cavity. Moreover, increasing the ventilation rate from 5.00×10^{-3} m^3 s^{-1} to 1.5×10^{-2} m^3 s^{-1} notably intensifies the instability within the cavity. Beyond the pronounced surface deformation, the enhanced mixing between the two phases at the interface further led to the entrapment of droplets from the surface

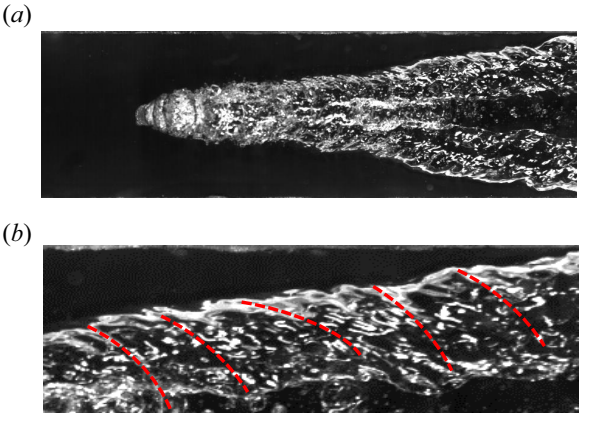

Figure 15. The experimental observation of (*a*) the interface instability in the BC regime and (*b*) the close-up view of the wavy structures on the branch for $D = 0.002$ m, $U_j = 127.33$ m s^{-1}, $U_\infty = 2$ m s^{-1}.

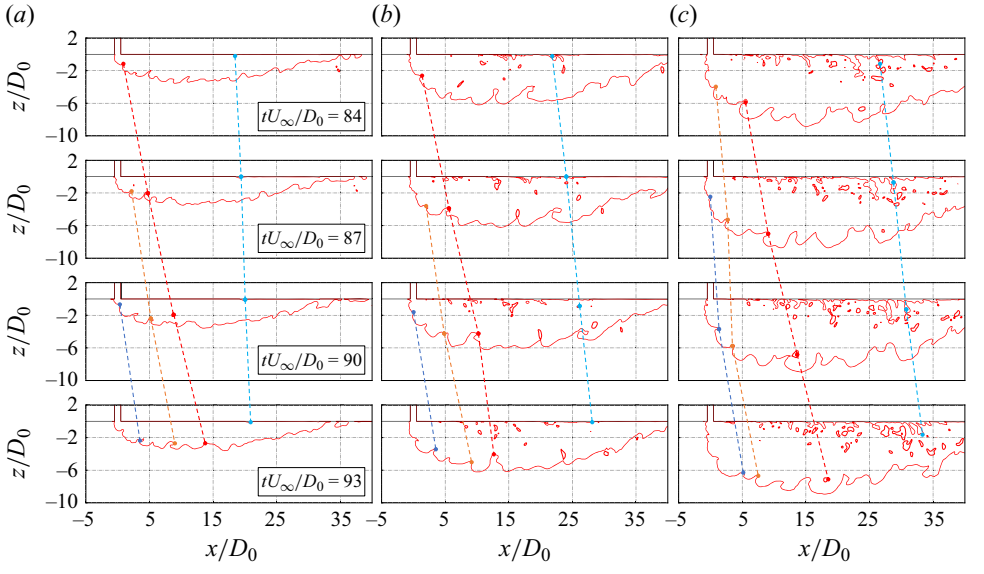

Figure 16. Instantaneous interface at the slice of $y/D_0 = 0$ at a series of time instants for (*a*) case 1, (*b*) case 8, and (*c*) case 9, with the movement of the Lagrangian points on the interface being monitored.

within the internal gas pocket, as evidenced by the trajectory of the Lagrangian points. The contour of the spatial and temporal distribution of the wall-normal velocity along the time-averaged interface, displayed in figure 17, reveals quantitatively the fluctuations of the cavity interface for the corresponding cases. The velocity oscillation commenced at approximately $x/D_0 = -1$, marginally ahead of the leading edge of the jet at $x/D_0 = -0.5$. The propagation pattern of the wall-normal velocity resembles that of a classical travelling wave, with a gradual attenuation in amplitude as it moves away from the origin. While the ventilation rate increases, the regularity of the velocity oscillation deteriorates, and the predominant frequency features maintain a relative constancy.

A comparison of the local frequency spectrum of wall-normal velocity is shown in figure 18, outlining the prevailing frequency and amplitude of interface fluctuations at

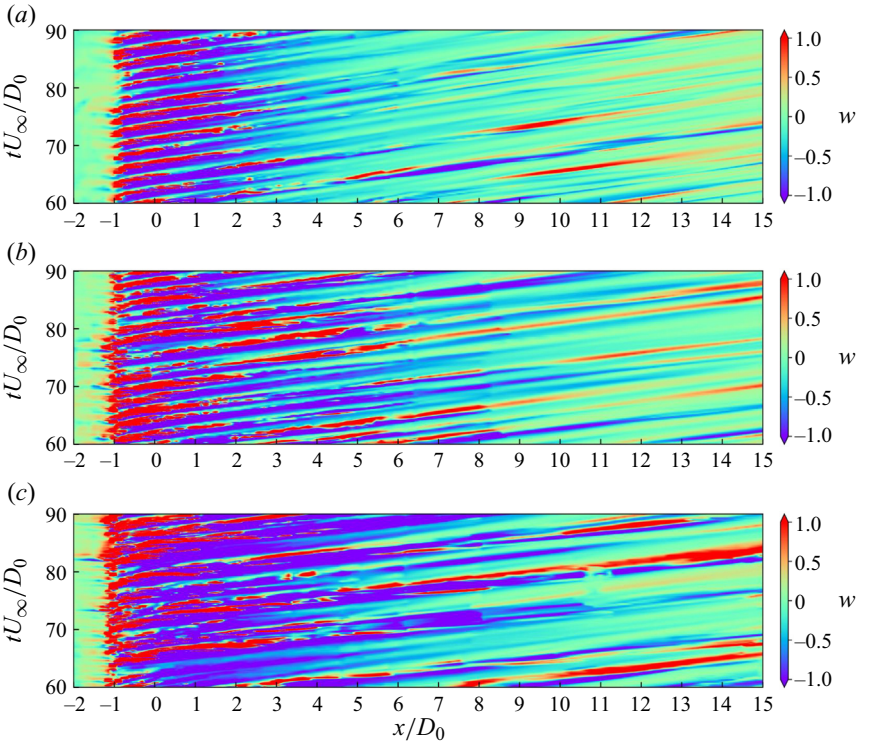

Figure 17. Spatial and temporal distributions of the wall-normal velocity along the time-averaged interface at the slice $y/D_0 = 0$ for (*a*) case 1, (*b*) case 8, and (*c*) case 9.

various cavity locations of a typical flow in the BC regime. At the leading edge of the orifice, the amplitude at the dominant frequency $f^* = fD/U_\infty$ exceeds 0.4, while the amplitudes at other adjacent peaks are also considerably high. It is conjectured that the observed multi-frequency traits may arise from the intricate interplay between the jet pressure within the orifice, the encroaching crossflow, and the surface tension on the dynamic contact line. The dominant frequency at $f^* = 0.33$ becomes more prominent than the other peaks at the position slightly downstream of the leading edge. In general, as the standoff distance from the orifice extends, there is a gradual decline in both the amplitude and the prevailing frequency of interface fluctuations within the puffing region. However, there is a marked disparity in the leading frequency when comparing the near-field region to the branches, with a steep descent from $f^* = 0.27$–0.41 to $f^* = 0.09$–0.11. Such a transformation in the leading frequency intimates a transition in the modes of instability, which will be discussed in detail below.

4.2. *The quantitative analyses by DMD*

The DMD method is utilized to discern the dominant frequency and corresponding global eigenmodes that dictate the instability of the ventilation cavity. Following the method of Schmid (2010), a sequence of stored flow fields with a constant time interval, $\boldsymbol{v}_i^N = \{\boldsymbol{v}_1, \boldsymbol{v}_2, \boldsymbol{v}_3, \ldots, \boldsymbol{v}_N\}$, can be decomposed into a linear combination of DMD modes

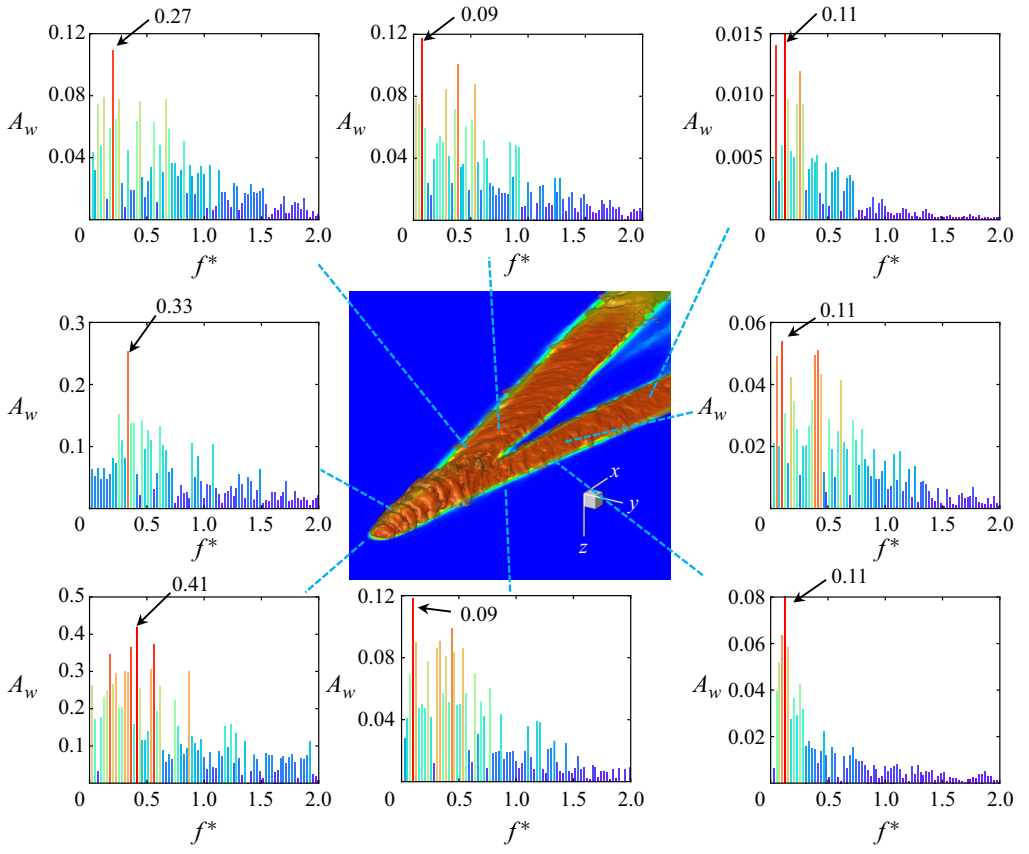

Figure 18. Local frequency spectrum of the wall-normal velocity measured on the different locations on the cavity interface of case 1, where the frequency is normalized by $f^* = fD/U_\infty$.

ϕ_i using singular value decomposition:

$$\boldsymbol{v}_i = \sum_{j=1}^{r} \phi_j (\lambda_j)^{i-1} A_j, \tag{4.1}$$

where A_j is the amplitude of each DMD mode ϕ_j, and the real and imaginary parts of the eigenvalue λ_j determine the growth rate and temporal frequency of the corresponding mode. The symbol r designates the truncation order for the DMD modes. In this subsection, we conducted DMD analyses on the numerical data from case 1, comprising 200 flow field snapshots taken at a consistent time increment $\Delta t = 0.5$ ms. Our sensitivity tests have confirmed that increasing the number or frequency of the samples would not affect the leading DMD modes of our interest. To investigate the flow instability near the orifice by DMD, we used only flow field data within the restricted subdomain $-10 < x/D_0 < 40$, enhancing computational efficiency and mitigating the memory requirement significantly.

Figure 19 shows the spectrum of (*a*) the growth rate and (*b*) the amplitude obtained from DMD for case 1. The predominant eigenmodes, marked by the yellow circles in the spectra at $f^* = 0.42$ and $f^* = 0.11$, manifest the most pronounced growth rates and amplitudes, with the exception of the zero-frequency time-averaged mode. By comparing the results

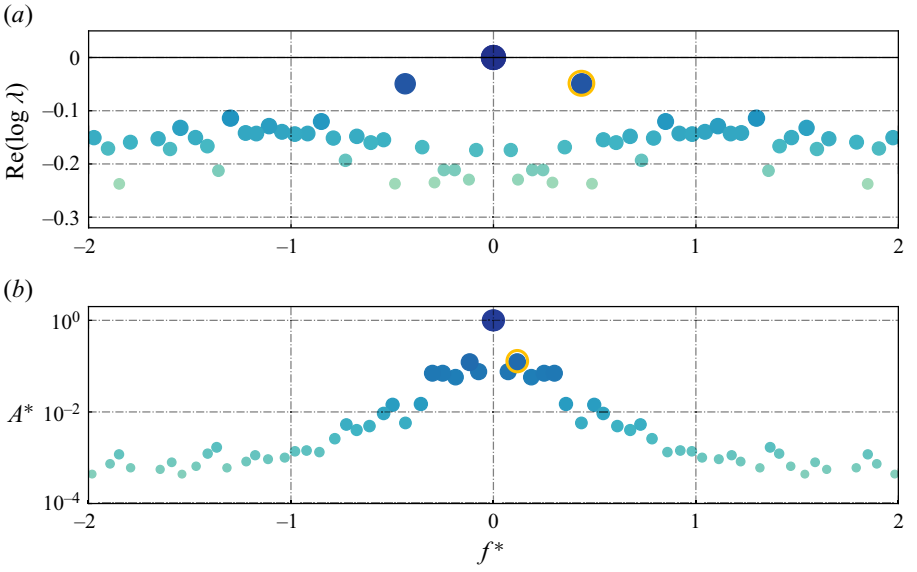

Figure 19. The spectrum of (*a*) the growth rate and (*b*) the amplitude of DMD modes for case 1, with the size and colour shading of the markers indicating the magnitude of the values for easy comparison.

with the local frequency spectrum shown in figure 18, we find that the former aligns closely with the peak frequency found near the orifice's leading edge, whereas the latter coincides with the downstream branch surface's fluctuating frequency. The DMD modes displayed in figure 20 extract the flow structures that underlie the most prominent interfacial instabilities observed in supplementary movie 2. The first perturbation mode triggering the puffing phenomenon is characterized by a short-wavelength and high-frequency disturbance, encapsulated by a ring-shaped wave structure. This mode is concentrated primarily near the orifice and attenuates rapidly after propagating to a position $x/D_0 \approx 18$. In contrast, the long-wavelength and low-frequency mode pervades the entire cavity surface, culminating in the highest amplitude observed. Upon the branch surfaces of the cavity, the disturbance waves display a discernible inclination relative to the crossflow rather than a perpendicular orientation. This tilt is ascribed to the more rapid velocity present on the cavity's inner surface relative to its outer surface.

4.3. *The mechanism for the onset of puffing phenomenon near the orifice*

The periodic pulsation of the ventilation cavity, known as the 'puffing' phenomenon, has been observed near the orifice not only in the case of the planar JICF discussed in this paper but also in the studies involving ventilation on a revolving body (Gan *et al.* 2022) and ventilated supercavitation (Jiang, Shao & Hong 2018). Consequently, this puffing phenomenon represents a prevalent yet under-examined instability in multiphase flows, emerging from the interplay between gas injections and liquid currents. In contrast to the Kelvin–Helmholtz instability in the parallel shear flow, the interface pulsations near the leading edge of the cavity are triggered predominantly by the localized and non-parallel interactions between the gas jet and the liquid crossflow.

Figure 21 presents a series of schematic diagrams that elucidate the underlying mechanism, which is evidenced by the static pressure contours displayed in the sub-figures, in conjunction with a comparison of the dynamic and static pressure within the cavity,

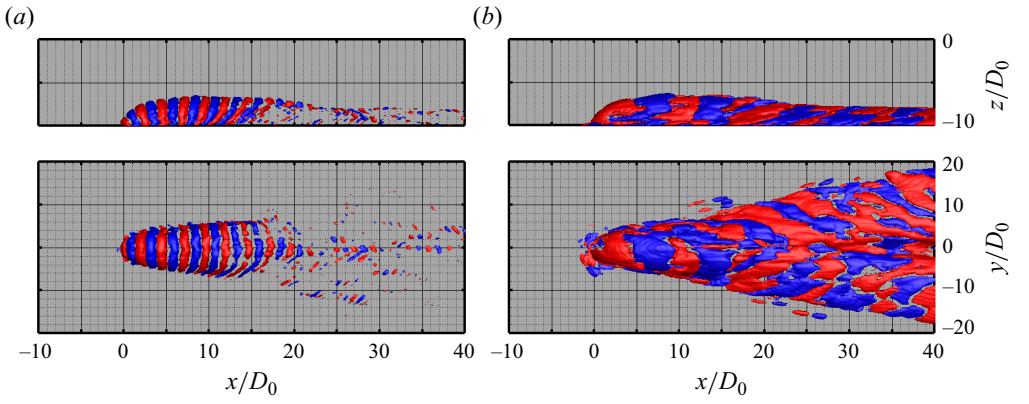

Figure 20. Isosurfaces of two leading DMD modes from the temporal series of volume fraction fields: (*a*) the largest growth rate at a non-zero frequency $f^* = 0.42$; and (*b*) the largest amplitude at a non-zero frequency $f^* = 0.11$.

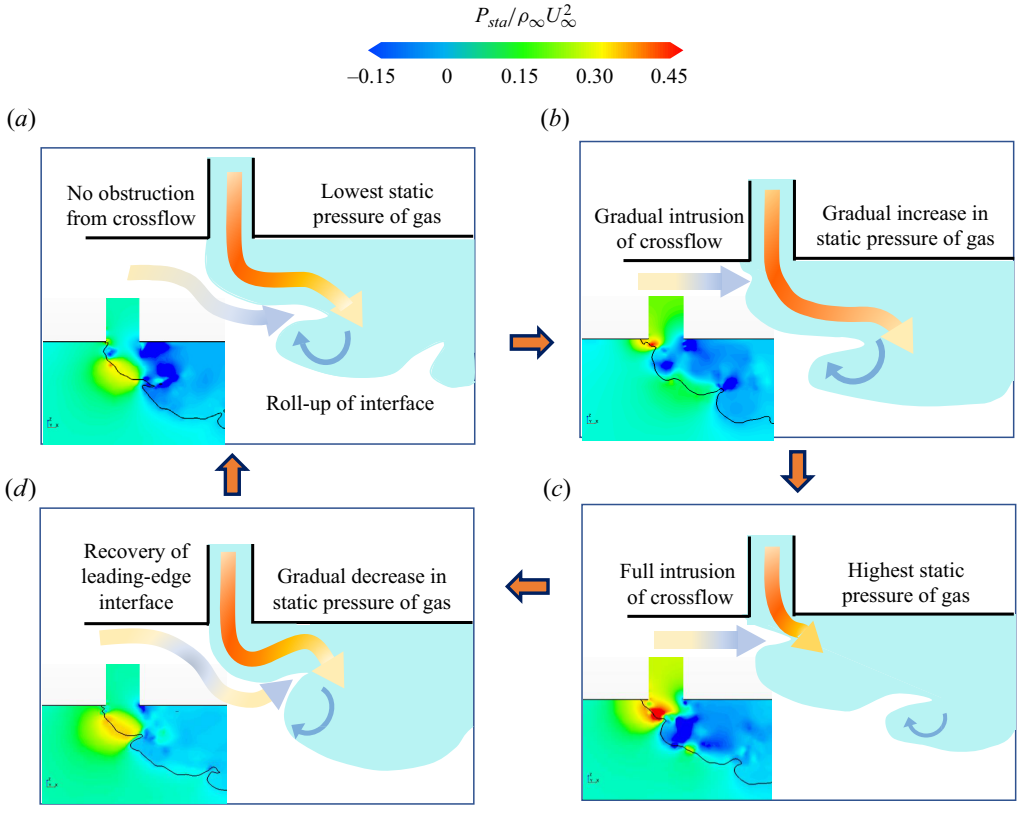

Figure 21. Schematic diagram to illustrate the development of the interfacial instability for the puffing phenomenon near the orifice, with the contours at the corners showing the static pressure at the corresponding instants.

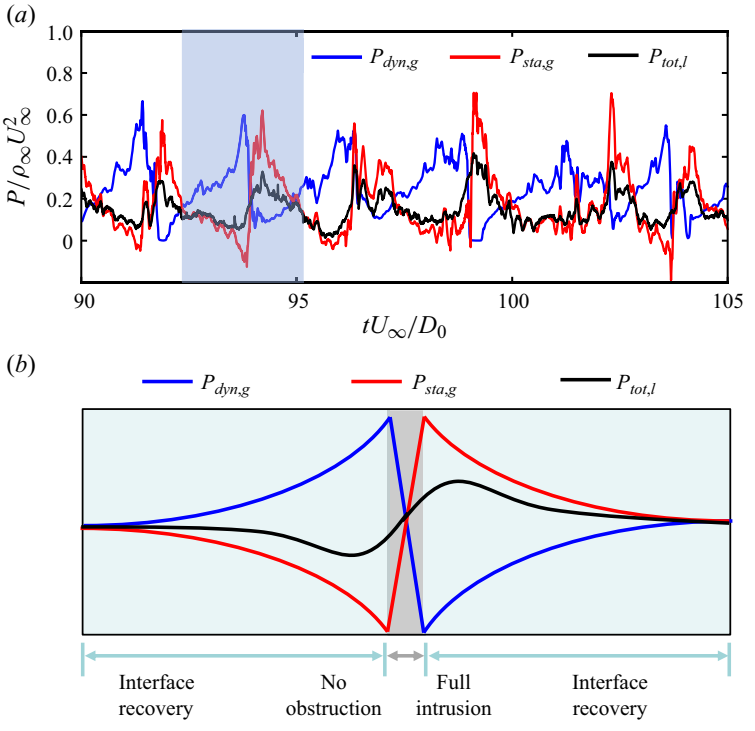

Figure 22. (*a*) Comparison of the instantaneous dynamic pressure $P_{dyn,g} = \rho_j \boldsymbol{u}^2/2$ and static pressure $P_{sta,g}$ within the cavity at $(x, y, z)/D_0 = (0.0, 0.0, -0.5)$, and the total pressure of liquid crossflow, $P_{tot,l} = P_{sta,l} + \rho_\infty \boldsymbol{u}^2/2$, slightly ahead of the cavity at $(x, y, z)/D_0 = (-1.0, 0.0, -0.5)$, which were obtained from case 1. (*b*) Sketch of the pressure variation related to different stages of one period.

and the total pressure of liquid crossflow at the respective monitoring points, as shown in figure 22. At the first instant (figure 21*a*), the gas injection is the least obstructed, with the low curvature on the leading edge of the cavity. However, the lowest static pressure due to the smooth gas injection is insufficient to counter the intrusion force of the crossflow. The obstruction of the gas cavity by the incoming liquid flow (figure 21*b*), on the other hand, leads to an increase in static pressure on the monitoring point, accompanied by a corresponding drop in dynamic pressure, given that the total pressure of the gas injection remains largely constant. Upon complete intrusion (figure 21*c*), the static pressure peaks while the dynamic pressure drops to its lowest, rendering the interface rebound under the overshooting pressure. The speed of interface recovery decelerates with the diminution of the overshooting pressure (figure 21*d*). The process of outward deforming ceases when the underpressure reappears and reaches its extreme again, thereby restoring the initial state discussed previously, and initiating a new cycle of the described sequence. It is also worth noting that the leading interface develops rapidly from no obstruction to full intrusion, while its recovery takes up the majority of the oscillation period.

According to the independent expansion principle (Logvinovich 1969), the evolution process of a cavitation bubble can be predicted qualitatively by the simplified one-dimensional equation by ignoring the surface tension and viscous force:

$$\frac{\partial^2 S(h,t)}{\partial t^2} = -\frac{k}{\rho}\,\Delta p(t), \tag{4.2}$$

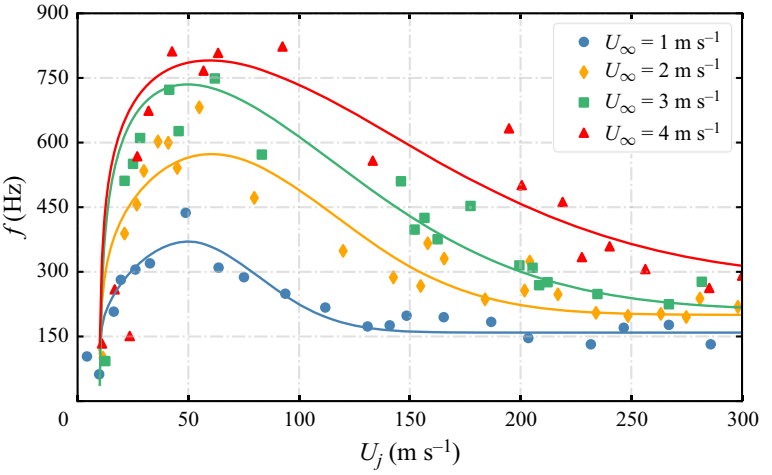

Figure 23. The leading frequency of puffing behaviour near the orifice with respect to different U_j and U_∞, which were obtained from experimental results for $D = 1$ mm.

where S denotes the instantaneous area of the cavity section with the normal to trajectory line, h is the curve coordinate system along the trajectory originating from the orifice, k is a coefficient affected by cavitation number, and Δp is the pressure difference across the cavity interface. By comparing the interface deformation shown in figure 21 and the corresponding instantaneous pressure at the monitoring point, we found that there is a phase lag between the cavity deformation and variation of pressure difference across the interface. The hysteresis phenomenon resembles the behaviours of the cavitation bubble predicted by (4.2), as described in Paryshev (2006). Therefore, we can infer that the puffing instability arises predominantly from the periodic oscillatory imbalance between the static pressure of gas near the orifice and the stagnation pressure of crossflow at the leading edge.

The variation of the leading frequency of the cavity pulsation in the near-field region with respect to jet velocity U_j is shown in figure 23 for four different crossflow velocities: $U_\infty = 1$, 2, 3 and 4 m s^{-1}. The results are derived from direct observations of films by the high-speed photography of the experimental results for $D = 1$ mm. The physical frequency, ascertained through direct measurements rather than the dimensionless Strouhal number, is provided to facilitate the discussion of the physical mechanisms involved. Generally, the pulsation frequency increases rapidly with the increase of U_j, and then gradually decreases. The highest frequency for crossflow $U_\infty = 1$–4 m s^{-1} increases from 437 Hz to 823 Hz. According to the flow regime shown in figure 5(a), the ventilation cavity is in the DB regime when the jet velocity is relatively low, and the corresponding frequency represents the detachment frequency of individual bubbles. In the DB regime, the time needed to form a new spherical bubble is dictated predominantly by the ventilation rate (or jet velocity), rendering the pulsation frequency largely unaffected by the crossflow velocity. The total pressure of the gas jet increases with the increase in jet velocity, which enhances the stability of the ventilation bubble. The detachment process of bubbles evolves from immediate severance to severance post a singular pulsation (as illustrated in figure 13), advancing to severance after several pulsations, and ultimately, it undergoes a gradual shift to the dynamics observed in the CC regime. The transitional process is similar to that in Rek *et al.* (2017), albeit their focus is on the upward gas injection against

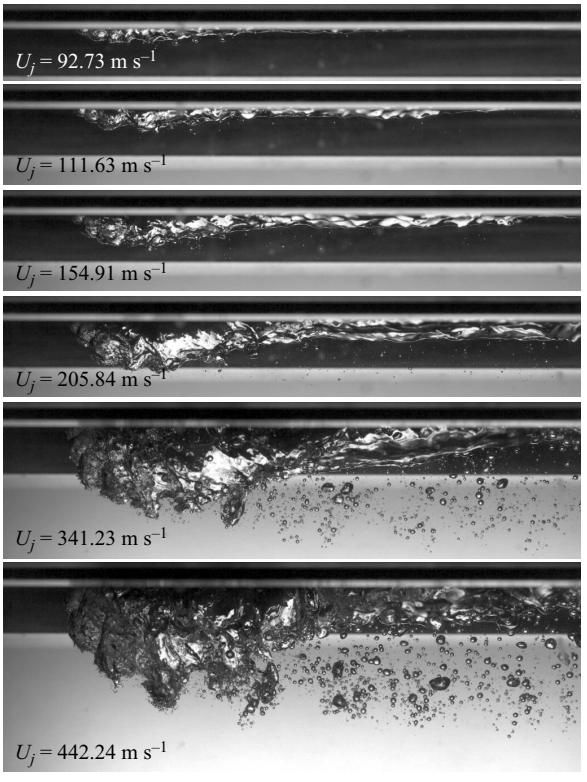

Figure 24. Snapshots of cavity topology development with an increase of U_j at $U_\infty = 2$ m s^{-1}, $D = 1$ mm, showing puffing instability at the higher U_j values. The corresponding animation is provided in supplementary movie 3.

a flat surface. Given that the period of the orifice pulsation is much shorter than the time required for the bubble to grow up, the dominant frequency of the cavity unsteadiness in the CC regime is much larger than that in the DB regime. Further increase in the jet velocity yields a rise in an increase in the total thickness of the cavity, while simultaneously elevating the static pressure within the injection pipe or near the orifice. As depicted in figure 24 and demonstrated in supplementary movie 3, the flow pattern evolves from CC to BC, and subsequently to BP, concurrent with an increase in jet velocity from 92.73 m s^{-1} to 442.24 m s^{-1}. When the crossflow intrusion descends, the magnitude of cavity fluctuations intensifies, and conversely, the frequency diminishes. Additionally, we have observed that the physical frequency of puffing increases with the increase of the crossflow velocity. The phenomenon is attributable to the inversely proportional decrease of the flow's characteristic time scale, denoted as $t_0 = D/U_\infty$, which diminishes concomitant with the increase of U_∞.

5. Conclusions

In this study, we investigated numerically and experimentally the flow characteristics and interfacial instabilities of the ventilation cavity induced by downward injecting into the liquid crossflow. Four distinct regimes of ventilation cavity and their transitional status are classified, which are mapped out on the parameter space spanned by crossflow velocity and jet velocity, derived from experimental data for two different orifice diameters.

The study examines thoroughly the interfacial instabilities of the ventilation cavity, utilizing both qualitative and quantitative methods to analyse the local and global spectrum features of pulsation. Furthermore, a theoretical framework has been established to elucidate the underlying mechanisms of the puffing phenomena observed in proximity to the orifice. The main conclusions are summarized as follows.

(i) The four typical flow regimes – discrete bubble (DB), continuous cavity (CC), bifurcated cavity (BC) and bubble plume (BP) – undergo a successive transition by increasing U_j, with the critical value of each regime boundary increasing nonlinearly as U_∞ increases.

(ii) Scaling effects exert a profound impact on cavity dynamics and interfacial stability, as fluctuations in characteristic length scale modify the Reynolds, Weber and Froude numbers. These dimensional changes govern turbulence intensity, bubble detachment and the gravitational forces influencing cavity bifurcation.

(iii) Two leading DMD modes were captured at high and low frequencies, respectively. The first perturbation mode characterized by a short-wavelength and high-frequency disturbance with a ring-like wave structure triggers the puffing phenomenon, which exhibits the highest growth rate. In contrast, the secondary mode, defined by a long wavelength and low frequency, permeates the entire cavity surface with the greatest amplitude.

(iv) The interface pulsation near the leading edge of the cavity is induced mainly by the local non-parallel flow between the gaseous jet and the liquid crossflow. A conceptual model is proposed to elucidate the dynamic process, which is governed mainly by the periodic oscillating imbalance between the static pressure of gas near the orifice and the stagnation pressure of crossflow at the leading edge.

Supplementary movies. Supplementary movies are available at https://doi.org/10.1017/jfm.2024.23.

Funding. The authors would like to acknowledge support from the Natural Science Foundation of Heilongjiang Province (no. YQ2022A004) and National Natural Science Foundation of China (nos 12372268, 51925904).

Declaration of interests. The authors report no conflict of interest.

Author ORCIDs.
Chengwang Xiong https://orcid.org/0000-0001-7029-1219;
A-Man Zhang https://orcid.org/0000-0003-1299-3049.

Appendix. Model validation

The convergence of mesh resolution is validated by a comparison of the time-averaged jet cavity profiles, with the set-ups listed in table 5. The minimum cell size for AMR dictated the resolution for the gas–liquid interface, while for the boundary layer, we employed a minimum cell size $\Delta x = 0.02D$, with D being the orifice diameter of different cases. The influence of the adaptive mesh size on the frequency distributions of the jet inlet pressure is shown in figure 25(*a*), which illustrates that the simulation with medium mesh resolution reaches acceptable consistency for the cavity interface. However, to better resolve the unsteady flow structures, we still choose the fine resolution for AMR throughout the paper. In addition, the frequency spectra of the gas pressure at the jet inlet obtained using three Courant numbers are compared in figure 25(*b*), The difference in the amplitude at the

Mesh	Minimum size for AMR	Total numbers of cells	Courant number
Fine	0.001 m	4.67×10^6	0.32
Medium	0.002 m	1.96×10^6	0.16
Coarse	0.003 m	1.05×10^6	0.11

Table 5. Numerical parameters of mesh convergence study for case 1.

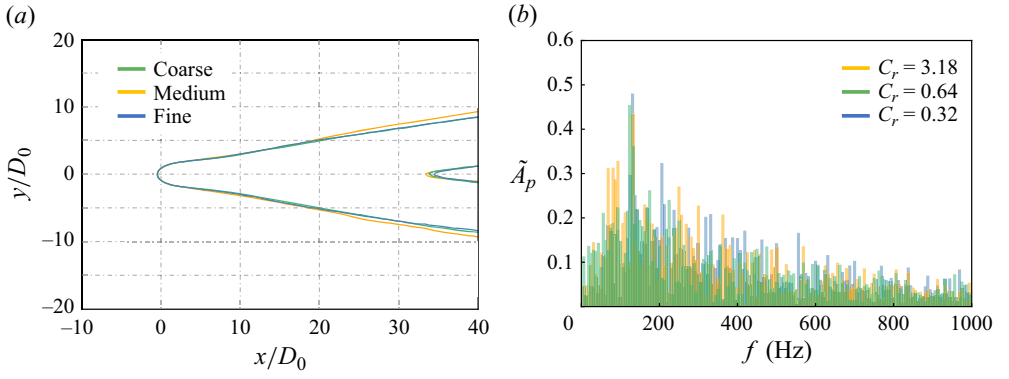

Figure 25. The validation tests for case 1: (*a*) the mesh convergence by a comparison of the time-averaged profile of cavity interface at $z = 0$; (*b*) the convergence of the Courant number by a comparison of the frequency spectrum of the gas pressure at the jet inlet.

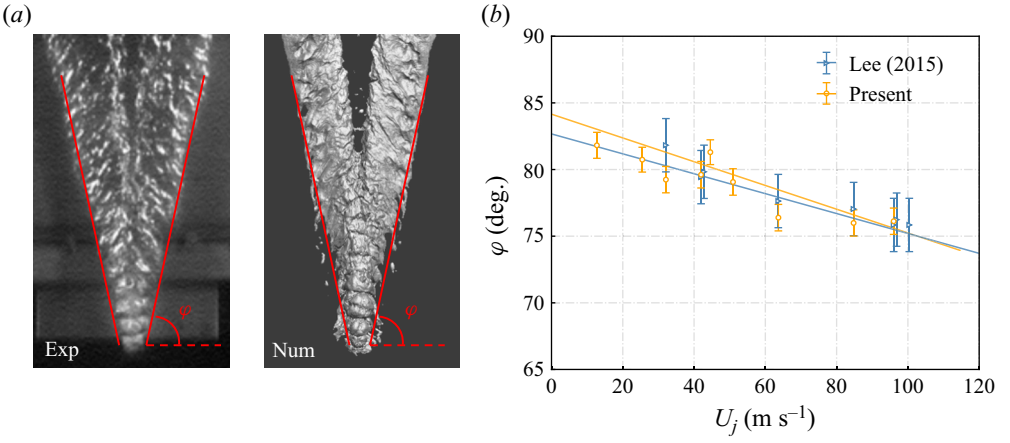

Figure 26. Comparison of the cavity topology between the experimental and present numerical results: (*a*) the experimental observation from Mäkiharju *et al.* (2017) and the present numerical visualization for case 1; (*b*) the sweep angle φ from the experimental data of Lee (2015) and the present simulations, with the error bar indicating the fitting error of φ.

dominant falls within 2 % between $C_r = 0.32$ and $C_r = 0.64$ indicating the convergence of the time step at $C_r = 0.32$.

Furthermore, the results from the present simulations are validated against the experimental results of Mäkiharju *et al.* (2017). Figure 26(*a*) compares the cavity morphology in the BC regime (case 1) against the experimental observation of

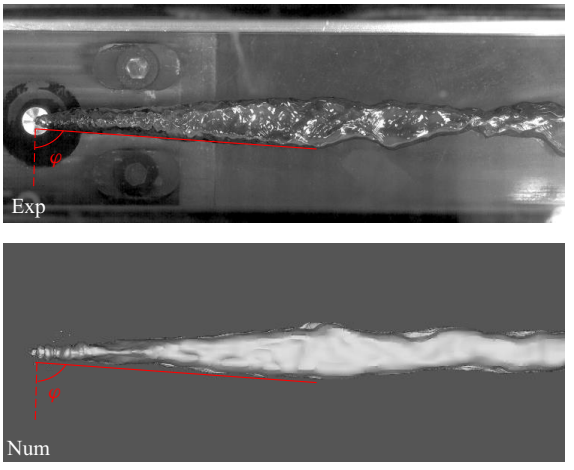

Figure 27. Comparison of the instantaneous cavity topology between the close-up view of the cavity obtained from the present experiment and the numerical results for $D = 1$ mm, $U_\infty = 3$ m s^{-1}, $U_j = 63.7$ m s^{-1}.

Mäkiharju *et al.* (2017). With the above mesh resolution, the near-field pinch-off phenomenon and the wavy structure on the gas branches can be captured well using the present numerical model. A comparison of the variation of the sweep angles with an increasing jet velocity is shown in figure 26(*b*), which suggests that the present numerical results agree well with the measured data from the experimental results of Lee (2015). Figure 27 further provides the validation of the instantaneous cavity topology between our experiment and numerical results for case 5, which shows good agreement as well. Additionally, we captured the dominant frequency of the near-field pulsating structure, $f = 750$ Hz, by the local frequency spectral analysis, which is well consistent with the value from our experiment measurement, $f = 748$ Hz.

References

Acharya, S., Tyagi, M. & Hoda, A. 2001 Flow and heat transfer predictions for film cooling. *Ann. N.Y. Acad. Sci.* **934** (1), 110–125.

Alves, L.S.B., Kelly, R.E. & Karagozian, A.R. 2008 Transverse-jet shear-layer instabilities. Part 2. Linear analysis for large jet-to-crossflow velocity ratio. *J. Fluid Mech.* **602**, 383–401.

Arora, P. & Saha, A.K. 2011 Three-dimensional numerical study of flow and species transport in an elevated jet in crossflow. *Intl J. Heat Mass Transfer* **54** (1), 92–105.

Bagheri, S., Schlatter, P., Schmid, P.J. & Henningson, D.S. 2009 Global stability of a jet in crossflow. *J. Fluid Mech.* **624**, 33–44.

Berger, M.J. & Colella, P. 1989 Local adaptive mesh refinement for shock hydrodynamics. *J. Comput. Phys.* **82**, 64–84.

Broumand, M., Birouk, M. & Mahmoodi, J.S.V. 2019 Liquid jet primary breakup in a turbulent cross-airflow at low Weber number. *J. Fluid Mech.* **879**, 775–792.

Ceccio, S.L. 2010 Friction drag reduction of external flows with bubble and gas injection. *Annu. Rev. Fluid Mech.* **42**, 183–203.

Chai, X., Iyer, P.S. & Mahesh, K. 2015 Numerical study of high speed jets in crossflow. *J. Fluid Mech.* **785**, 152–188.

Choi, K.W., Lai, C.C.K. & Lee, J.H.W. 2016 Mixing in the intermediate field of dense jets in cross currents. *J. Hydraul. Engng ASCE* **142**, 04015041.

Cortelezzi, L. & Karagozian, A.R. 2001 On the formation of the counter-rotating vortex pair in transverse jets. *J. Fluid Mech.* **446**, 347–373.

Dong, P., Lu, B., Gong, S. & Cheng, D. 2020 Experimental study of submerged gas jets in liquid cross flow. *Exp. Therm. Fluid Sci.* **112**, 109998.

DONG, P., WANG, K., CHENG, D. & LU, B. 2021 Submerged gas jet in liquid cross flow: modeling and flow structures analysis. *Ocean Engng* **242**, 110128.

ELBING, B.R., MÄKIHARJU, S.A., WIGGINS, A., PERLIN, M., DOWLING, D.R. & CECCIO, S.L. 2013 On the scaling of air layer drag reduction. *J. Fluid Mech.* **717**, 484–513.

FRIC, T.F. & ROSHKO, A. 1994 Vortical structure in the wake of a transverse jet. *J. Fluid Mech.* **279**, 1–47.

GAN, N., YAO, X., CHENG, S., CHEN, Y. & MA, G. 2022 Experimental investigation on dynamic characteristics of ventilation bubbles on the surface of a vertical moving body. *Ocean Engng* **246**, 110641.

GEVORKYAN, L., SHOJI, T., PENG, W.Y. & KARAGOZIAN, A.R. 2018 Influence of the velocity field on scalar transport in gaseous transverse jets. *J. Fluid Mech.* **834**, 173–219.

GRUBER, M.R., NEJAD, A.S., CHEN, T.H. & DUTTON, J.C. 1997 Compressibility effects in supersonic transverse injection flowfields. *Phys. Fluids* **9** (5), 1448–1461.

HAKKI, I., INSEL, M. & HELVACIOGLU, I. 2010 Flow analysis of an air injection through discrete air lubrication. In *International Conference on Ship Drag Reduction 2010*.

HIRT, C.W. & NICHOLS, B. 1981 Volume of fluid (VOF) method for the dynamics of free boundaries. *J. Comput. Phys.* **39**, 201–225.

ILAK, M., SCHLATTER, P., BAGHERI, S. & HENNINGSON, D.S. 2012 Bifurcation and stability analysis of a jet in cross-flow: onset of global instability at a low velocity ratio. *J. Fluid Mech.* **696**, 94–121.

JIANG, Y., SHAO, S. & HONG, J. 2018 Experimental investigation of ventilated supercavitation with gas jet cavitator. *Phys. Fluids* **30** (1), 012103.

KELSO, R.M., LIM, T.T. & PERRY, A.E. 1996 An experimental study of round jets in cross-flow. *J. Fluid Mech.* **306**, 111–144.

LEE, I.R. 2015 Scaling of gas diffusion into limited partial cavity and interaction of vertical jet with cross-flow beneath horizontal surface. PhD thesis, The University of Michigan.

LOGVINOVICH, G.V. 1969 Hydrodynamics of flows with free boundaries. PhD thesis, Naukova Dumka, Kiev.

MAHESH, K. 2013 The interaction of jets with crossflow. *Annu. Rev. Fluid Mech.* **45** (1), 379–407.

MÄKIHARJU, S.A. & CECCIO, S.L. 2018 On multi-point gas injection to form an air layer for frictional drag reduction. *Ocean Engng* **147**, 206–214.

MÄKIHARJU, S.A., LEE, I.R., FILIP, G.P., MAKI, K.J. & CECCIO, S.L. 2017 The topology of gas jets injected beneath a surface and subject to liquid cross-flow. *J. Fluid Mech.* **818**, 141–183.

MARSHALL, S.H. 1992 Air bubble formation from an orifice with liquid cross-flow. PhD thesis, University of Sydney.

MEYER, K.E., PEDERSEN, J.M. & ÖZCAN, O. 2007 A turbulent jet in crossflow analysed with proper orthogonal decomposition. *J. Fluid Mech.* **583**, 199–227.

MIRSANDI, H., SMIT, W.J., KONG, G., BALTUSSEN, M.W., PETERS, E.A.J.F. & KUIPERS, J.A.M. 2020 Bubble formation from an orifice in liquid cross-flow. *Chem. Engng J.* **386**, 120902.

NICOUD, F. & DUCROS, F. 1999 Subgrid-scale stress modelling based on the square of the velocity gradient tensor. *Flow Turbul. Combust.* **62**, 183–200.

PARYSHEV, E. 2006 Approximate mathematical models in high-speed hydrodynamics. *J. Engng Maths* **55**, 41–64.

PATANKAR, S.V. & SPALDING, D.B. 1972 A calculation procedure for heat, mass and momentum transfer in three-dimensional parabolic flows. *Intl J. Heat Mass Transfer* **15**, 1787–1806.

PEPLINSKI, A., SCHLATTER, P. & HENNINGSON, D.S. 2015 Global stability and optimal perturbation for a jet in cross-flow. *Eur. J. Mech. (*B*/Fluids)* **49**, 438–447.

PESCINI, E., FRANCIOSO, L., DE GIORGI, M.G. & FICARELLA, A. 2015 Investigation of a micro dielectric barrier discharge plasma actuator for regional aircraft active flow control. *IEEE Trans. Plasma Sci.* **43** (10), 3668–3680.

PETERSON, S.D. & PLESNIAK, M.W. 2004 Evolution of jets emanating from short holes into crossflow. *J. Fluid Mech.* **503**, 57–91.

REGAN, M.A. & MAHESH, K. 2017 Global linear stability analysis of jets in cross-flow. *J. Fluid Mech.* **828**, 812–836.

REGAN, M.A. & MAHESH, K. 2019 Adjoint sensitivity and optimal perturbations of the low-speed jet in cross-flow. *J. Fluid Mech.* **877**, 330–372.

REK, Z., GREGORC, J., BOUAIFI, M. & DANIEL, C. 2017 Numerical simulation of gas jet in liquid crossflow with high mean jet to crossflow velocity ratio. *Chem. Engng Sci.* **172**, 667–676.

ROWLEY, C.W., MEZIĆ, I., BAGHERI, S., SCHLATTER, P. & HENNINGSON, D.S. 2009 Spectral analysis of nonlinear flows. *J. Fluid Mech.* **641**, 115–127.

SAÏD, N.M., MHIRI, H., PALEC, G.L. & BOURNOT, P. 2005 Experimental and numerical analysis of pollutant dispersion from a chimney. *Atmos. Environ.* **39** (9), 1727–1738.

SCHLÜTER, J. & SCHÖNFELD, T. 2000 LES of jets in cross flow and its application to a gas turbine burner. *Flow Turbul. Combust.* **65**, 177–203.

SCHMID, P.J. 2010 Dynamic mode decomposition of numerical and experimental data. *J. Fluid Mech.* **656**, 5–28.

SCHMID, P.J. 2022 Dynamic mode decomposition and its variants. *Annu. Rev. Fluid Mech.* **54**, 225–254.

SHOJI, T., HARRIS, E.W., BESNARD, A., SCHEIN, S.G. & KARAGOZIAN, A.R. 2020 On the origins of transverse jet shear layer instability transition. *J. Fluid Mech.* **890**, A7.

SILBERMAN, E. & SONG, C.S. 1961 Instability of ventilated cavities. *J. Ship Res.* **5** (2), 13–33.

SOCOLOFSKY, S.A. & ADAMS, E.E. 2002 Multi-phase plumes in uniform and stratified crossflow. *J. Hydraul. Res.* **40** (6), 661–672.

THIELICKE, W. & STAMHUIS, E.J. 2014 PIVlab – towards user-friendly, affordable and accurate digital particle image velocimetry in MATLAB. *J. Open Res. Softw.* **2** (1), e30.

VIGNEAU, O., PIGNOUX, S., CARREAU, J.L. & ROGER, F. 2001 Influence of the wall boundary layer thickness on a gas jet injected into a liquid crossflow. *Exp. Fluids* **30** (4), 458–466.

WACE, P.F., MORRELL, M.S. & WOODROW, J. 1987 Bubble formation in a transverse horizontal liquid flow. *Chem. Engng Commun.* **62** (1–6), 93–106.

WANG, L., HUANG, B., QIN, S., CAO, L., FANG, H., WU, D. & LI, C. 2020 Experimental investigation on ventilated cavity flow of a model ship. *Ocean Engng* **214**, 107546.

ZHANG, A.-M., LI, S.-M., CUI, P., LI, S. & LIU, Y.-L. 2023 A unified theory for bubble dynamics. *Phys. Fluids* **35**, 033323.